Research Article Vol. 2, No. 6 / 25 December 2024 / Optica Quantum 475

OPTICA QUANTUM

Overcoming the fundamental limit of quantum transduction via intraband entanglement

Haowei Shi[1,3] and Quntao Zhuang[1,2,4]

[1]Ming Hsieh Department of Electrical and Computer Engineering, University of Southern California, Los Angeles, California 90089, USA
[2]Department of Physics and Astronomy, University of Southern California, Los Angeles, California 90089, USA
[3]haow.shi@gmail.com
[4]qzhuang@usc.edu

Received 4 September 2024; revised 14 November 2024; accepted 22 November 2024; published 20 December 2024

A quantum transducer converts an input signal to an output probe at a distant frequency band while maintaining the quantum information with high fidelity, which is crucial for quantum networking and distributed quantum sensing and computing. In terms of microwave–optical quantum transduction, the state-of-the-art quantum transducers suffer low transduction efficiency from weak nonlinear coupling, wherein increasing pump power to enhance efficiency inevitably leads to thermal noise from heating. Moreover, we reveal that the efficiency-bandwidth product of a cavity electro-optical or electro-optomechanical transducer is fundamentally limited by pump power and nonlinear coupling coefficient, irrespective of cavity engineering efforts. To overcome this fundamental limit, we propose to noiselessly boost the transduction efficiency by consuming intraband entanglement (e.g., microwave–microwave or optical–optical entanglement in the case of microwave–optical transduction). Via a squeezer–coupler–antisqueezer sandwich structure, the protocol enhances the transduction efficiency to unity in the ideal lossless case, given an arbitrarily weak pump and nonlinear coupling. In practical cavity systems, our entanglement-assisted protocol surpasses the non-assisted fundamental limit of the efficiency-bandwidth product and reduces the threshold cooperativity for positive quantum capacity by a factor proportional to two-mode squeezing gain. Given a fixed cooperativity, our approach increases the broadband quantum capacity by orders of magnitude. The entanglement-assisted advantage is robust to ancilla loss and cavity detuning.

https://doi.org/10.1364/OPTICAQ.540881

1. INTRODUCTION

Quantum transduction aims to interconnect quantum computers and processors via converting quantum states between different frequencies [1–3]. It serves as the hinge between the microwave superconducting qubits and the optical telecommunication photons, enabling robust quantum networking [4–7], and ultimately distributed quantum sensing [8] and distributed quantum computing [9,10]. Despite the proposals based on various physical platforms [11–27], current quantum transduction systems are still far from satisfying, hurdled by a conundrum to balance transduction efficiency, pump-induced heating, and bandwidth [26,28–32].

An ideal transducer has unity transduction efficiency, zero added noise, and large bandwidth. As one-way quantum communication is forbidden for efficiency below 50% [33], remarkable efforts have been made to improve the on-resonance transduction efficiency to >50%. For example, the recent progress in electro-optomechanical transducers [11,34] adopts extremely high-Q mechanical resonators as a mediating mode to connect the microwave mode and the optical mode, which achieves the highest transduction efficiency up to 47% so far with 3.2 noise photons [30]. However, such mediation boosts the on-resonance efficiency at the cost of bandwidth, e.g., the bandwidth is limited to 2 kHz in Ref. [30], cf. typical bandwidth ~ 10 MHz of direct conversion [28,29,35]. Indeed, the bandwidth of an electro-optomechanical transducer is limited below the mechanical resonance frequency, approximately megahertz, which must operate at the resolved sideband limit to suppress the undesired blue sideband two-mode squeezing noise [30,36]. Gigahertz piezo-optomechanical transducers [19,26] offer room-temperature broadband transduction, but the transduction efficiency is limited, e.g., ~ 10^{-5} in Refs. [19,26], due to the optical absorption heating of mechanical resonators [37]. The direct electro-optical conversion [15,16] is free from the complications due to the mechanical mode, whereas its transduction efficiency is still limited [17,28]. Pulsed pumping has been demonstrated to mitigate the heating and further boost the instantaneous nonlinear coupling for piezo-optomechanical transduction [26] and direct electro-optical transduction [29,35], however, its low duty cycle drastically reduces the transduction rate and it is incompatible with continuous-wave signals.

Such a trade-off between the transduction efficiency and bandwidth is inevitable. In this paper, we reveal that the efficiency-bandwidth product (EBP) [38] of cavity electro-optical or electro-optomechanical transduction, and any transduction with similar Hamiltonian, is fundamentally limited by the nonlinear

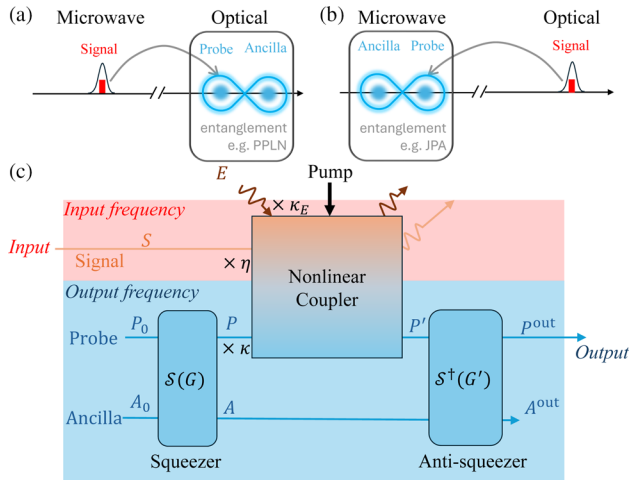

Fig. 1. Schematic of the EA transduction protocol. (a) EA microwave-to-optical transduction, enhanced by optical entanglement which can be generated by PPLN [57]. (b) EA optical-to-microwave transduction, enhanced by microwave entanglement which can be generated by JPA [53–55]. (c) Detailed protocol. An input signal S is converted to an output probe P^{out} at a different frequency. The probe and ancilla are initially cooled to vacuum state, and two-mode squeezed by $\mathcal{S}(G)$ of gain G. Then, the signal is cast onto the probe by a nonlinear coupler, which is modelled as a beam splitter of transmissivity κ, signal–probe conversion efficiency η, and loss $\kappa_E = 1 - \kappa - \eta$. Finally the probe and ancilla are antisqueezed by $\mathcal{S}^\dagger(G')$, the probe is output while the ancilla is discarded.

coupling coefficient and pump amplitude, regardless of the linewidths of cavities. Unfortunately, the nonlinear coupling between photons is intrinsically weak, and a stronger pump inevitably induces more thermal noise [37]. Therefore, besides the endeavor in materials science and nanofabrication, paradigm shifts are needed to boost quantum transduction and overcome the limit.

Recently, there have been theoretical efforts toward this goal. For example, one can utilize the conventionally discarded environment output to correct the transducer imperfection, via adaptive control [39] or Gottesman–Kitaev–Preskill (GKP) encoding [40]. However, the adaptive control protocol relies on ultra-precise broadband homodyne measurement and adaptive displacement in addition to inline squeezing; the state-of-the-art systems for GKP state engineering [41] are far from usable. In addition, the GKP qubit encoding of the input quantum information is not compatible with continuous variables. Other approaches rely on crossband microwave–optical entanglement [32,42] to enable the teleportation-based transduction approach [25,43]; however, noiseless teleportation requires high fidelity crossband entanglement and thus extremely high pump power along with the heating issue as challenging as the direct frequency conversion.

In this work, we propose an intraband-entanglement-assisted protocol to achieve a noiseless broadband enhancement in the efficiency of bosonic transduction between arbitrary distant frequencies, therefore overcome the fundamental limitation on EBP. Adopting techniques from entanglement-assisted (EA) weak signal sensing [44] and nonlinear interferometry [45,46], the proposed protocol only requires intraband (optical–optical or microwave–microwave) entanglement as shown in Figs. 1(a) and 1(b), distinct from teleportation which requires crossband entanglement, measurement, and conditional operation. In the absence of loss, for an arbitrarily weak nonlinear coupling, the transduction efficiency can always be enhanced up to unity without any added noise. In the next section, we provide an overview of the protocol and its EA advantage.

2. OVERVIEW

Entanglement assistance is known as a powerful resource that enhances the precision of weak signal detection beyond the standard quantum limit (SQL) in various scenarios, e.g., nonlinear interferometry [46,47], quantum illumination radar [48], and dark matter search [44,49], via combining two-mode squeezing and antisqueezing before and after the sensing process. The EA advantage has been demonstrated experimentally using photonic ancilla [50,51] and spin ancilla [52]. In this paper, we exploit entanglement assistance to boost quantum transduction.

The EA protocol is shown in Fig. 1. Our protocol features an ancilla entangled with the output at the same frequency band, e.g., at the optical or microwave band for microwave–optical transduction as shown in Figs. 1(a) and 1(b). The entanglement is generated via an intraband two-mode squeezer $\mathcal{S}$ before the traditional nonlinear coupling, and processed by an antisqueezer $\mathcal{S}^\dagger$ afterwards, as shown in Fig. 1(c). Such intraband entanglement is much easier to implement than the crossband entanglement required in teleportation-based transducers [25,43]. For example, microwave squeezers have been well established via a Josephson parametric amplifier (JPA) [53–55]. Optical entanglement has been readily generated using potassium titanyl phosphate [56] and periodically poled lithium niobate (PPLN) [57], while optical inline squeezers are also being actively developed [58,59]. While we explicitly consider optical–microwave transduction in Figs. 1(a) and 1(b), in Fig. 1(c) we choose not to specify the input and output frequencies in our protocol, since the protocol allows general bosonic transduction, including phonon–photon conversion [60].

The pumped nonlinear coupler can be described by a linearized input–output relation, specifically a two-mode bosonic Gaussian channel which can be categorized into beam-splitter-type or two-mode-squeezing-type depending on the pump detuning, for both the cavity electro-optic coupling [16] and the cavity electro-optomechanical coupling [61]. Our analysis focuses on beam-splitter-type nonlinear couplers, of which the pumps are red-detuned, which avoid the two-mode squeezing noise [30,36] and allow noiseless quantum transduction.

The performance of noiseless quantum transduction is characterized by the signal-to-probe photon conversion efficiency $\eta(\omega)$, as a function of the signal frequency ω. The broadband performance can be quantified by the EBP

$$\mathcal{B} \equiv \int_{-\infty}^{\infty} \eta(\omega) d\omega \tag{1}$$

or the broadband quantum capacity [62–66]

$$Q_1 = \int \frac{d\omega}{2\pi} \max\left[\log_2\left(\frac{\eta(\omega)}{1-\eta(\omega)}\right), 0\right], \tag{2}$$

of which fundamental limits can be proven for beam-splitter-type quantum transducers. In terms of EBP, we prove fundamental limits in Section 4.1 (see Theorem 2 and Theorem 3), as summarized in Theorem 1.

Theorem 1 (Informal overview). *The EBP of an electro-optical transducer $\mathcal{B}$ is upper-bounded by $\mathcal{B} \le \pi|g\alpha|$, limited by the nonlinear coupling coefficient g and in-cavity pump power $|\alpha|^2$, regardless of cavity linewidths. Enhanced by a mechanical mediating mode, the EBP of an electro-optomechanical transducer is still upper-bounded similarly by nonlinear coupling coefficients and pump power.*

Such fundamental limits hold for any nonlinear couplings of similar Hamiltonians. In terms of the quantum capacity, it is known that cooperativity of the electro-optical transduction cavity needs to overcome a threshold $C_{\rm th} = 3 - 2\sqrt{2}$ to enable any non-zero capacity [43]. These fundamental limits create a conundrum in balancing pump power and heating in quantum transduction engineering.

Our main result is that these fundamental limits can be overcome by utilizing intraband entanglement. In the simple beam splitter model of nonlinear coupling, the squeezer–coupler–antisqueezer protocol allows noiseless amplification [45] of the nonlinear coupling, capable of boosting an arbitrarily low transduction efficiency to unity. Such EA noise reduction in parametric amplification has been demonstrated in experiments [67,68]. In the full cavity model, in terms of the quantum capacity, the cooperativity threshold can be lowered by a factor of $C_{\rm th,EA} \sim 1/G$ proportional to the two-mode squeezing gain G, relaxing the requirement of cavity engineering drastically. In terms of EBP, the proposed EA transduction protocol enables $\mathcal{B}_{\rm EA} \sim G \cdot \mathcal{B}$, allowing a factor of G advantage in EBP.

Our paper is organized as follows. We begin with the simple beam splitter model of coupling in Section 3 to introduce the core mechanism of the protocol and analyze the advantage at a single frequency. Then, we connect the beam splitter model to the physical cavity model in Section 4, where we derive the fundamental limits on transduction and show that these limits can be overcome by intraband entanglement. Several appendices addressing robustness of our protocol to experimental imperfections are noteworthy: Appendix A, Section 2 addresses losses in two-mode squeezing operations which can be simplified to ancilla storage loss, where robustness to loss is observed; Appendix A, Section 4 addresses imperfect pump detunings, where robustness to large detuning is identified; Appendix A, Section 5 addresses the implementation of frequency-dependent squeezing, where a sequential array of cavity parametric amplifiers is shown to approach the required squeezing spectrum.

3. BEAM SPLITTER MODEL OF COUPLING

3.1. Protocol Design

As shown in Fig. 1(c), a general bosonic transducer converts an input signal S to an output probe P' at different frequency bands via a nonlinear coupler. A general model for such coupler is a frequency-dependent beam splitter [11,16,34,61]. Given a specific input frequency, the coupling can be modelled by a beam splitter [69]. Without entanglement assistance, the transduction efficiency is limited by the signal–probe photon conversion efficiency $0<\eta\ll 1$. The transmissivity of the initial probe P is $\kappa \le 1-\eta$, as an environment port E is inevitably mixed in with transmissivity (the intrinsic loss) $\kappa_E = 1-\kappa-\eta \ge 0$. Its input–output relation in the Fourier frequency domain is

$$\hat{\mathcal{E}}_{P'} = e^{i\theta_P}\sqrt{\kappa}\hat{\mathcal{E}}_P + e^{i\theta_S}\sqrt{\eta}\hat{\mathcal{E}}_S + \sqrt{\kappa_E}\hat{\mathcal{E}}_E, \tag{3}$$

where θ_P, θ_S are phase shifts during the coupling. Here $\hat{\mathcal{E}}_X(\omega)$ is the traveling-wave field operator of system X at frequency ω relative to its own carrier, satisfying the commutation relation $[\hat{\mathcal{E}}_X(\omega), \hat{\mathcal{E}}_X^\dagger(\omega')] = \delta(\omega-\omega')$. In this section, we focus on the beam splitter model at a single frequency and omit ω for simplicity, while the broadband case will be discussed later in the full cavity model. We will connect such a beam splitter model to the physical cavity electro-optics and electro-optomechanical systems in Section 4.

To enhance the overall quantum transduction efficiency from the input to the output, we amplify the signal-carrying probe while keeping the noise background in a vacuum state. To suppress the noise, we introduce an ancilla A. The ancilla and the probe run a "squeezer–coupler–antisqueezer" protocol with a sandwich structure for the transducer: first the probe P and the ancilla A are cooled to vacuum states and entangled by a two-mode squeezer with gain G; then, a portion η of the signal S is converted to the probe P' via nonlinear coupling; finally, the converted probe P' and the ancilla A are antisqueezed with gain G' to produce the final converted output $P^{\rm out}$. The squeezer and the antisqueezer are set to null the probe back to vacuum when the input is vacuum. In the main text, we ignore the loss in the squeezer and antisqueezer, as they operate on the probe–ancilla pair at close frequencies (e.g., both in the microwave frequencies [53–55]) thus it is much easier to engineer than the signal–probe coupler. We analyze the impact of squeezing loss in Appendix A, Section 2, which shows that the advantage of our EA protocol is robust against the loss in squeezing and ancilla storage.

Below, we elaborate this protocol step by step. Before the signal–probe coupling, we prepare the probe and the ancilla using a two-mode squeezer $\mathcal{S}(G)$ of gain G on initial vacuums P_0 and A_0. The input–output relation can be conveniently expressed via the linear transform of the field operators

$$\begin{aligned}\hat{\mathcal{E}}_P &= \sqrt{G}\hat{\mathcal{E}}_{P_0} + \sqrt{G-1}\hat{\mathcal{E}}_{A_0}^\dagger,\\ \hat{\mathcal{E}}_A &= \sqrt{G-1}\hat{\mathcal{E}}_{P_0}^\dagger + \sqrt{G}\hat{\mathcal{E}}_{A_0}.\end{aligned} \tag{4}$$

After the two-mode squeezing, the signal is coupled to the probe via the nonlinear coupler as described by Eq. (3). Finally, the probe and the ancilla are antisqueezed using $\mathcal{S}^\dagger(G')$ to output

$$\hat{\mathcal{E}}_{P^{\rm out}} = e^{-i\theta_P}\sqrt{G'}\hat{\mathcal{E}}_{P'} - \sqrt{G'-1}\hat{\mathcal{E}}_A^\dagger, \tag{5}$$

where the phase is chosen to cancel the transduction phase shifts θ_P in Eq. (3). The full formula of the overall input–output relation can be found as Eq. (A.3) in Appendix A, Section 1. To minimize the transduction noise, we solve G' to keep the output to vacuum when the input signal is vacuum, which gives

$$G' \leftarrow G'^\star \equiv \frac{1}{1-\kappa+\kappa/G}. \tag{6}$$

In this case, the noise background in the output probe is vacuum

$$\hat{\mathcal{E}}_{P^{\rm out}}^\star = \sqrt{\eta_{\rm EA}}e^{i(\theta_S-\theta_P)}\hat{\mathcal{E}}_S + \sqrt{1-\eta_{\rm EA}}\hat{\mathcal{E}}_{\rm VAC}, \tag{7}$$

where the background $\hat{\mathcal{E}}_{\rm VAC}$ is in a vacuum state, and

$$\eta_{\rm EA} = \eta G'^\star = \eta\frac{G}{G(1-\kappa)+\kappa}, \tag{8}$$

is the noiseless EA transduction efficiency. It is noteworthy that the transduction efficiency enhancement holds even if the probe and ancilla are initially in thermal states, wherein the background $\hat{\mathcal{E}}_{\rm VAC}$ will be in a thermal state instead.

One can regard the two-mode antisqueezer $\mathcal{S}^\dagger(G')$ as an amplifier of the probe, while the first input two-mode squeezer $\mathcal{S}(G)$

reduces the amplifier noise [45,67] from the antisqueezer. Equation (6) indicates that to increase the signal amplification G' noiselessly, the input squeezer gain G needs to increase accordingly to suppress the amplification noise. Below, our analysis begins with the ideal lossless case where $\kappa_E = 0$ and then proceeds to the lossy case of $\kappa_E > 0$.

3.2. Lossless Coupler: Unity-Efficiency Transduction

Now we assume the lossless limit $\kappa_E = 0$ to gain intuition about the protocol design, which is always true at the cavity overcoupling limit (see Section 4). In this case, $\kappa = 1 - \eta$ and the optimal gain in Eq. (6) reduces to $G' \leftarrow G'^{\star} \equiv 1/[\eta + (1-\eta)/G]$. The EA transduction efficiency is

$$\eta_{\mathrm{EA}}|_{\kappa_E=0} = \eta \cdot \frac{G}{G\eta + (1-\eta)}, \tag{9}$$

which approaches unity in the strong squeezing limit,

$$\eta_{\mathrm{EA}}|_{\kappa_E=0} \to 1, \text{when} G' \to 1/\eta \text{ and } G \to \infty. \tag{10}$$

At this limit, the output probe $\hat{\mathcal{E}}^{\star}_{P\mathrm{out}} = e^{i(\theta_S-\theta_P)}\hat{\mathcal{E}}_S$ is reflectionless in both quadratures. Although the reflectionless transduction requires infinite squeezing in Eq. (10), the EA advantage is still significant at finite squeezing. For a finite gain, the EA protocol increases the efficiency to $\eta_{\mathrm{EA}} \simeq G\eta$ by the amplifier gain factor G, at the weak nonlinear coupling limit $\eta \ll 1$. Note that here no-cloning [70] is not violated because the other output of the nonlinear coupler is infinitely noisy at the $G \to \infty$ limit. The intuition behind such an enhancement is that the ancilla A provides a reference entangled with the quantum fluctuation in the probe P after the two-mode squeezer $\mathcal{S}(G)$. At the limit $G \to \infty$, the quadratures of the two modes are fully correlated as $\mathrm{Re}\hat{\mathcal{E}}_P = \mathrm{Re}\hat{\mathcal{E}}_A, \mathrm{Im}\hat{\mathcal{E}}_P = -\mathrm{Im}\hat{\mathcal{E}}_A$ [69]. Thus, the antisqueezer $\mathcal{S}^{\dagger}(G')$ can noiselessly amplify the signal transduced into P', where the quantum noise from A during the antisqueezing interference can be completely cancelled utilizing the remaining entanglement. At the lossless limit, the signal is perfectly recovered.

To enable quantum communication with one-way quantum capacity $Q_1 > 0$, one needs the overall conversion efficiency above the zero-quantum-capacity threshold, $\eta_{\mathrm{EA}} > 1/2$ [33], leading to $\eta > 1/(G+1)$ which is drastically easier to achieve than the non-EA case of $\eta > 1/2$.

3.3. Lossy Coupler

Here we consider general case with intrinsic loss $\kappa_E > 0$. In the strong squeezing limit, the EA transduction efficiency Eq. (8) goes to

$$\eta_{\mathrm{EA}} \to \frac{1}{1 + \kappa_E/\eta}, \text{ when } G' \to 1/(1-\kappa) \text{ and } G \to \infty. \tag{11}$$

The challenging non-EA zero-quantum-capacity threshold $\eta > 1/2$ is relaxed to the EA threshold $\eta > \kappa_E$ now, which is always achievable via overcoupling the cavity.

We evaluate the EA advantage in transduction efficiency in Fig. 2. In Fig. 2(a), we fix the intrinsic loss $\kappa_E = 0.01$ and vary the non-EA efficiency η. The EA efficiency overwhelms the non-EA efficiency (blue diagonal line), even with an intermediate-scale, near-term available squeezing gain $G = 10$ dB. In the inset, we observe the EA efficiency η_{EA} surpasses the zero-quantum-capacity threshold 1/2 (upper boundary of blue-shaded region)

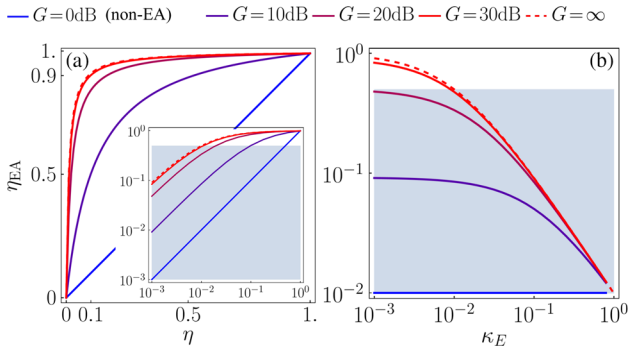

Fig. 2. The EA transduction efficiency η_{EA} versus (a) the non-EA efficiency η, with $\kappa_E = 0.01$ and (b) the intrinsic loss κ_E, with $\eta = 0.01$. Inset in (a) is the zoom-in near $\eta \to 0$ in logarithmic scale. Squeezer gain G, from blue to red; G increases from 0dB (non-EA) to 30 dB by step of 10 dB. Red dashed, $G \to \infty$ [Eq. (11)]. Blue-shaded region, zero quantum-capacity region $\eta_{\mathrm{EA}} \le 1/2$. Antisqueezer gain G' is chosen according to Eq. (6).

at $\eta \gtrsim \kappa_E = 0.01$, given squeezing gain $G = 30$ dB—as predicted by Eq. (11). In Fig. 2(b), we fix $\eta = 0.01$ and vary κ_E. At high squeezing, the zero-quantum-capacity threshold $\eta_{\mathrm{EA}} = 1/2$ can be achieved for $\kappa_E \lesssim \eta = 0.01$. For the minimum squeezing requirement, we observe that at least $G = 20$ dB is required for $\eta_{\mathrm{EA}} \ge 1/2$ in the best case $\kappa_E \to 0$, which can be predicted by the lossless coupler, Eq. (9).

4. FULL CAVITY MODEL OF COUPLING

Now we proceed to the full cavity model for the nonlinear couplers. Without loss of generality, here we present the formulation of cavity electro-optical coupling. A similar formulation of cavity electro-optomechanical coupling [11,34] is included in Appendix A, Section 6, which holds for general bosonic nonlinear coupling with a mediating mode.

In cavity electro-optics, probe P and signal S are carried on optical/microwave cavity modes, associated with annihilation operators $\hat{a}_P, \hat{a}_S$ satisfying the commutation relation $[\hat{a}_X, \hat{a}_X^{\dagger}] = 1$, where $X = P, S$. The quality of the cavities are characterized by the cavity external coupling rates and intrinsic loss rates $\gamma_{X,c}$ and $\gamma_{X,0}$. In this paper, we adopt the alternative characterization with the total linewidths $\Gamma_X \equiv \gamma_{X,c} + \gamma_{X,0}$ and the coupling ratios $\zeta_X \equiv \gamma_{X,c}/\Gamma_X$. Here we consider the perfectly red-detuned pump for simplicity [15,16], e.g., for microwave-to-optical transduction the optical pump frequency is perfectly at $\omega_{\mathrm{pump}} = \omega_P - \omega_S$, where ω_P, ω_S are the cavity resonance frequencies of the optical probe and microwave signal, respectively. We defer the general formulation allowing imperfect pump detuning to Appendix A, Section 4, which demonstrates that our protocol is robust against the detuning imperfections. In the frame rotating with the cavity resonance frequencies, assuming the rotating wave approximation, an electro-optics system in the red sideband pumping case can be described by the effective Hamiltonian [15,16],

$$\hat{H}_I = -\hbar g(\alpha^* \hat{a}_S^{\dagger}\hat{a}_P + \alpha \hat{a}_S \hat{a}_P^{\dagger}), \tag{12}$$

where g is the electro-optic nonlinear coupling coefficient in hertz and α is the in-cavity pump amplitude. The interaction strength is typically characterized by the cooperativity $C = 4|g\alpha|^2/\Gamma_S\Gamma_P$.

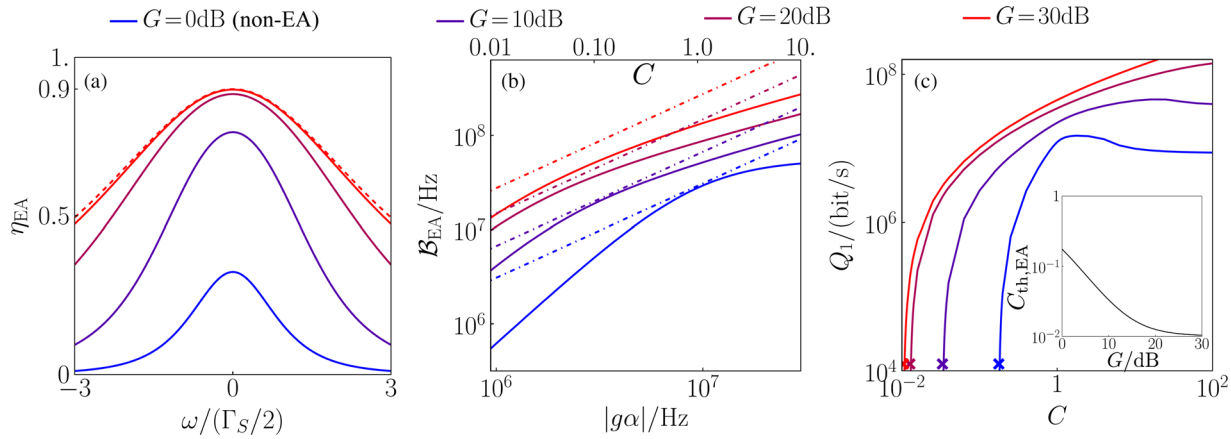

Fig. 3. (a) The EA transduction efficiency spectrum $\eta_{\rm EA}(\omega)$ under various squeezing gain G. Cooperativity $C = 0.1$. The dashed line is the $G \to \infty$ limit obtained from Eq. (15). (b) The EA EBP $\mathcal{B}_{\rm EA}$ versus the effective nonlinear coupling strength $|g\alpha|$. The solid lines are under fixed Γ_P, Γ_S, for which we provide the cooperativity C values as the upper axis ticks; while the dot–dashed lines are under optimized Γ_P, Γ_S that maximize $\mathcal{B}_{\rm EA}$ for a given $|g\alpha|$. (c) Broadband quantum capacity rate Q_1 versus cooperativity C under various squeezing gain G. The crosses indicate the zero-quantum-capacity thresholds $C_{\rm th}$ under each G in Eq. (19). Inset is $C_{\rm th,EA}$ versus G(dB), as given in Eq. (19). The $G = 0$ dB point goes back to Eq. (18). In all figures, $\zeta_P = \zeta_S = 0.99$; linewidths $\Gamma_P = 25.8$ MHz, $\Gamma_S = 13.706$ MHz are chosen according to the high-cooperativity setup in Ref. [29], except the dot–dash lines of (b).

Solving the steady-state solution of the quantum Langevin equation [16,71] for $\hat{H}_I$ in the Fourier domain, we obtain the broadband version of Eq. (3). The probe transmissivity spectrum is

$$\sqrt{\kappa(\omega)}e^{i\theta_P(\omega)} = -1 + \frac{2\zeta_P(1-2i\frac{\omega}{\Gamma_S})}{(1-2i\frac{\omega}{\Gamma_P})(1-2i\frac{\omega}{\Gamma_S})+C}, \tag{13}$$

the signal-to-probe transduction efficiency spectrum is

$$\sqrt{\eta(\omega)}e^{i\theta_S(\omega)} = \frac{2i\sqrt{C}\sqrt{\zeta_P\zeta_S}}{(1-2i\frac{\omega}{\Gamma_P})(1-2i\frac{\omega}{\Gamma_S})+C}. \tag{14}$$

As a reminder, here ω is in the frame rotating with the cavity resonance frequencies. The intrinsic loss spectrum can be obtained correspondingly as $\kappa_E(\omega) = 1 - \kappa(\omega) - \eta(\omega)$. It is worthwhile to note that the cavity is asymptotically lossless ($\kappa_E(\omega) \to 0$) at the cavity overcoupling limit ($\zeta_P, \zeta_S \to 1$). For weak nonlinear coupling $C \ll 1$, the peak conversion efficiency $\eta(\omega = 0) = \zeta_P\zeta_S \cdot 4C/(1+C)^2$; the half-power bandwidth of $\eta(\omega)$ is $B \simeq \min\{\Gamma_S, \Gamma_P\}$.

Now we demonstrate the EA advantage. For simplicity, we assume a broadband two-mode squeezing for the squeezer $G(\omega) = G$; for the gain in the antisqueezing, however, the optimal choice of phase matching $\theta_P(\omega)$ and gain $G'^{\star}(\omega)$ in Eq. (6) will be frequency dependent. Nevertheless, these requirements can be achieved by properly engineering the squeezing cavities, e.g., using a sequential array of parametric amplifiers as we present in Appendix A, Section 5. In particular, frequency-dependent squeezing is already being utilized in the Laser Interferometer Gravitational-Wave Observatory (LIGO) [72,73]. According to Eq. (8), the EA transduction efficiency is $\eta_{\rm EA}(\omega) = \eta(\omega)\, G/[G\,(1-\kappa(\omega)) + \kappa(\omega)]$. At the $G \to \infty$ limit, we obtain a closed-form expression

$$\eta_{\rm EA}(\omega)|_{G\to\infty} = \frac{C\Gamma_S^2\zeta_S}{\Gamma_S^2\,(C+1-\zeta_P) + 4\omega^2\,(1-\zeta_P)}. \tag{15}$$

With entanglement assistance, we observe an improvement in the peak efficiency $\eta_{\rm EA}(\omega = 0)|_{G\to\infty} = \zeta_S/[1 + (1-\zeta_P)/C]$, and a bandwidth broadening $B_{\rm EA}|_{G\to\infty} = \sqrt{1 + C/(1-\zeta_P)}\Gamma_S$. Remarkably, the EA bandwidth no longer depends on the probe linewidth Γ_P at $G \to \infty$. Hence the EA advantage is not limited to the weak nonlinear coupling scenarios: even though the on-resonance efficiency can get close to unity with stronger pumping, entanglement allows broadband improvement via bandwidth broadening. Similar quantum advantages using non-classical probes have been found in cavity dark matter searches [44,74].

We plot an example of the EA conversion efficiency spectrum $\eta_{\rm EA}(\omega)$ in Fig. 3(a). As predicted, we see that the bandwidth of the non-EA case ($G = 0$ dB) is approximately Γ_S, and the EA bandwidth grows as G increases in addition to the peak efficiency advantage.

In the following, we quantify the EA advantage with three measures of transduction performance: EBP, minimum threshold of cooperativity for quantum communication, and broadband quantum capacity.

4.1. Fundamental Limit on EBP

To quantify the broadband transduction efficiency, we define EBP as the integral of transduction efficiency over the entire spectrum [see Eq. (1)]. This metric is particularly useful for broadband quantum sensing applications [44].

Theorem 2 (The EBP limit for electro-optical transduction). *Without entanglement assistance, the EBP of quantum transduction with Hamiltonian* Eq. (12) *[which leads to lineshape* $\eta(\omega)$, Eq. (14)*] is*

$$\mathcal{B} \equiv \int_{-\infty}^{\infty}\eta(\omega)d\omega = \frac{2\pi C\Gamma_P\Gamma_S\zeta_P\zeta_S}{(C+1)(\Gamma_P+\Gamma_S)} \le \mathcal{B}_{\rm max}, \tag{16}$$

which achieves the maximum $\mathcal{B}_{\rm max} \equiv \pi\zeta_S\zeta_P|g\alpha| \le \pi|g\alpha|$, *at* $\Gamma_P = \Gamma_S = 2|g\alpha|$ *(i.e.,* $C = 1$*) given a fixed* $|g\alpha|$.

The full derivation is in Appendix A, Section 3. Here $\mathcal{B}_{\rm max}$ is a fundamental limit for the non-EA case determined by the nonlinear coupling coefficient g and pump power $\propto |\alpha|^2$, which is independent on any higher-Q cavity engineering. For electro-optomechanical transducers, we present a similar limit in Subsection 4.3.

Meanwhile, we also derive a closed-form expression of EA EBP $\mathcal{B}_{\rm EA} \equiv \int_{-\infty}^{\infty} \eta_{\rm EA}(\omega) d\omega$, which is too lengthy to be displayed here. Under the same cavity setup $\Gamma_P = \Gamma_S = 2|g\alpha|$, $\zeta_P = \zeta_S = 1$, we obtain $\mathcal{B}_{\rm EA} = G^{1/4}\pi|g\alpha| \geq G^{1/4}\mathcal{B}_{\rm max}$, breaking the fundamental limit $\mathcal{B}_{\rm max}$ of the non-EA case. Allowing freely choosing $\Gamma_P = \Gamma_S = 2\sqrt{G}|g\alpha|$, we have $\mathcal{B}_{\rm EA} \simeq 0.703\sqrt{G}\pi|g\alpha|$ with $\sqrt{G}$ advantage compared with $\mathcal{B}_{\rm max}$. When $G \to \infty$,

$$\mathcal{B}_{\rm EA}|_{G\to\infty} \to \frac{\pi C \Gamma_S \zeta_S}{2\sqrt{(1+C-\zeta_P)(1-\zeta_P)}}, \tag{17}$$

which diverges as $\zeta_P \to 1$ as expected.

While the above optimal results provide the ultimate limits, here we also consider the practical case of low cooperativity $C \ll 1$. In this case, entanglement can enhance EBP by a factor of G, $\mathcal{B}_{\rm EA} = G \cdot \mathcal{B}$ when $\zeta_P = \zeta_S = 1$.

Under imperfect $\zeta_P, \zeta_S < 1$, we plot $\mathcal{B}_{\rm EA}$ in Fig. 3(b). Still, we observe orders of magnitude of EA advantage. Either with Γ_S, Γ_P fixed (solid lines), or with optimized Γ_S, Γ_P over each given $|g\alpha|$ (dot–dashed lines), the EA advantages are demonstrated over the maximal non-EA EBP $\mathcal{B}_{\rm max}$ (blue dot–dashed line) over a wide range of effective nonlinear coupling strength $|g\alpha|$, corresponding to cooperativity $C \in [0.01, 10]$ for the Γ_S, Γ_P fixed cases.

4.2. Threshold of Cooperativity and Broadband Quantum Information Rate

While the EBP provides an intuitive characterization of the transduction efficiency, the ultimate quantum information transmission rates are characterized by the quantum capacity [62–64] across the entire spectrum. When the environment is cooled to vacuum, the one-way quantum capacity of transducer is given by Eq. (2) [65,66].

At the weak nonlinear coupling limit, the maximum transduction efficiency locates at the on-resonance frequency $\omega = 0$. For the non-EA case, we have $\eta(0) = 4C\zeta_P\zeta_S/(1+C)^2$ which surpasses the zero-capacity threshold $1/2$ only when [43]

$$C \geq C_{\rm th} = -1 + 4\zeta_S\zeta_P - \sqrt{8\zeta_S\zeta_P(2\zeta_S\zeta_P - 1)} \geq 3 - 2\sqrt{2}. \tag{18}$$

With the EA boost, we have the threshold

$$\begin{aligned} C_{\rm th,EA} =& -1 + \zeta_P\left((4\zeta_S - 2)\,G + 2\right) \\ & - 2\sqrt{\zeta_P G\left(\zeta_P\left(4\zeta_S + (1-2\zeta_S)^2 G - 1\right) - 2\zeta_S\right)}. \end{aligned} \tag{19}$$

When $G \to \infty$, the threshold converges to $C_{\rm th} \to (1-\zeta_P)/(2\zeta_S - 1)$ when $\zeta_S \geq 1/2$.

Additional insight can be obtained by considering the overcoupling limit of $\zeta_P = \zeta_S = 1$, threshold in Eq. (19) leads to $C_{\rm th,EA}|_{\zeta_P=\zeta_S=1} = 1/(\sqrt{G} + \sqrt{1+G})^2$, which is lowered by a factor of $1/G$ asymptotically. It is easy to check that $\eta_{\rm EA}(0)$ approaches unity at the large G limit. We plot the threshold in the inset of Fig. 3(c) for a practical case and identify a reduction by over an order of magnitude when squeezing gain G is large.

We plot Q_1 versus the cooperativity C for different gain G in Fig. 3(c). Merely $G = 10$ dB squeezing is sufficient to enable orders of magnitude advantage at low cooperativity. Remarkably, for large C the quantum capacity without probe–ancilla entanglement begins to decay with C as the cavity goes into the oscillatory region with Rabi splitting; in contrast, the quantum capacity assisted by probe–ancilla entanglement can further increase with $C \gg 1$.

4.3. Generalization to Transduction with Intermediate Modes

Microwave–optical quantum transduction is known to be enhanced by mediating modes. As an example, we focus on the electro-optomechanical transduction, which yields the state-of-the-art efficiency so far [30]. In the frame rotating at the cavity resonance frequencies for microwave and optical modes, the cavity electro-optomechanical dynamics can be described by the effective Hamiltonian [11,71,75]

$$H_I = \hbar g_S \hat{a}_S^\dagger \hat{a}_S \hat{x}_M + \hbar g_P \hat{a}_P^\dagger \hat{a}_P \hat{x}_M, \tag{20}$$

where $\hat{a}_S, \hat{a}_P, \hat{a}_M$ are the annihilation operators of the signal (microwave/optical), probe (optical/microwave), and mediating (mechanical) modes, and $\hat{x}_M = x_{\rm zp}(\hat{a}_M + \hat{a}_M^\dagger)$ with $x_{\rm zp} = \sqrt{\frac{\hbar}{2m\omega_M}}$ being the zero-point motion. The mechanical oscillator has mass m and frequency ω_M. Here the nonlinear coupling coefficients g_S, g_P are in units of hertz per meter. We define $\mathcal{G}_{S,P} \equiv g_{S,P} x_{\rm zp}|\alpha_{S,P}|$ proportional to the nonlinear coupling coefficients and pumping amplitudes, analogous to $g|\alpha|$ in the electro-optical coupling [16].

Consider red sideband pumping and the resolved sideband limit, the electro-optomechanical coupling yields the beam-splitter-type input–output relation similar to the electro-optics, up to a different spectral lineshape. Thus, most of our conclusions for the electro-optics can be trivially generalized to the electro-optomechanics. Here we present the EBP limit.

Theorem 3 (The EBP limit for electro-optomechanical transduction). *Without entanglement assistance, the EBP of quantum transduction with Hamiltonian* Eq. (20) *is upper-bounded by* Eq. (A.42) *as a function of* $\mathcal{G}_P, \mathcal{G}_S$.

Specifically, in the symmetric case of $\mathcal{G}_P = \mathcal{G}_S = \mathcal{G}$, *the EBP is upper-bounded by*

$$\mathcal{B}_{\mathcal{G}_P=\mathcal{G}_S} \leq \frac{\sqrt{107 + 51\sqrt{17}}}{32}\pi\zeta_P\zeta_S\mathcal{G} \simeq 1.749\zeta_P\zeta_S\mathcal{G}. \tag{21}$$

The full derivation is in Appendix A, Section 6b.

Our EA transduction protocol also applies to electro-optomechanical transduction. Similar enhancement in EBP proportional to two-mode squeezing gain G can overcome the above fundamental EBP limit. At the overcoupling limit $\zeta_P, \zeta_S \to 1$ and lossless mechanical resonator, the overall coupling loss $\kappa_E(\omega) \to 0$, then the signal can always be perfectly recovered with strong squeezing $G \to \infty$ as $\eta_{\rm EA}(\omega)|_{\kappa_E\to 0, G\to\infty} \to 1$.

5. DISCUSSION

The most challenging part of the proposed EA transduction is the frequency-dependent inline squeezing. In the optical-to-microwave transduction, the required microwave inline squeezing can be readily realized to high gain [53–55]. Alternative to realizing optical inline squeezing for microwave-to-optical transduction, one can also utilize the optical-to-microwave transduction to generate optical–microwave entanglement from optical–optical entanglement [76,77], then teleportation enables bi-directional transduction [25,43,78]. We present a simple frequency-dependent antisqueezer design using a sequential array of cavity parametric amplifiers in Appendix A, Section 5, which approaches the desired antisqueezing spectrum well and achieves scalable advantage in the broadband quantum capacity over the non-EA transduction.

In this paper we have focused on the beam-splitter-type nonlinear couplers. We expect the intraband entanglement to similarly enhance the squeezing-type couplers, which we leave for future study. We note that the squeezing-type transducers cannot perform any quantum transduction without our proposal of intraband entanglement assistance, because it forms a phase-conjugate amplifier of zero quantum capacity [61,79].

Compared with the proposal with in-cavity squeezing [80] that boosts a single quadrature transduction, our approach allows transduction of both quadratures, and thus is free from encoding in the ideal case, and does not require additional pumping at the cavity that can lead to additional heating. We note that the in-cavity squeezing protocol [80] requires the cavity system to be on resonance with minimal detuning, resulting in a highly limited operating bandwidth. In contrast, our protocol is robust against the detunings (as shown in Section 4 and Appendix A, Section 4b) and is only subject to frequency-independent requirements of relatively low intrinsic loss (achievable by overcoupled cavities) and strong squeezing, thus enabling broadband transduction. Moreover, an explicit protocol that recovers the initial quantum state is absent in Ref. [80]. Compared with the GKP-based protocol in Ref. [40] that requires the input signal to be GKP encoded, our protocol relies on less challenging quantum resources of inline squeezing. Distinct from both the two protocols above, our proposal lifts the requirement of encoding and thus can be applied to transduce general bosonic quantum states more compatible with existing optical communication infrastructures. While Ref. [40] only considers the perfect cavity of $\kappa_E = 0$, our protocol shows advantage for general scenarios. Compared with the adaptive protocol [39], our protocol does not require the precise broadband homodyne measurement and adaptive control which include delay lines that increase the loss, and limit the capacity and speed of transduction. We note that our proposal requires two-mode squeezers, similar to the single-mode squeezers in Ref. [39], of which the bandwidth is being actively increased [55,57,81].

APPENDIX A

1. Full Derivation of the Overall Input–Output Relation of the EA Transducer

Consider initial probe and ancilla modes $\hat{\mathcal{E}}_{P_0}, \hat{\mathcal{E}}_{A_0}$ in vacuum. The two-mode squeezer before nonlinear coupling gives

$$\begin{aligned}\hat{\mathcal{E}}_P &= \sqrt{G}\hat{\mathcal{E}}_{P_0} + \sqrt{G-1}\hat{\mathcal{E}}^\dagger_{A_0},\\ \hat{\mathcal{E}}_A &= \sqrt{G-1}\hat{\mathcal{E}}^\dagger_{P_0} + \sqrt{G}\hat{\mathcal{E}}_{A_0}.\end{aligned} \tag{A.1}$$

The nonlinear coupling forms a beam splitter between the squeezed probe $\hat{\mathcal{E}}_P$ and the signal $\hat{\mathcal{E}}_S$,

$$\hat{\mathcal{E}}_{P'} = e^{i\theta_P}\sqrt{\kappa}\hat{\mathcal{E}}_P + e^{i\theta_S}\sqrt{\eta}\hat{\mathcal{E}}_S + \sqrt{\kappa_E}\hat{\mathcal{E}}_E, \tag{A.2}$$

while ancilla $\hat{\mathcal{E}}_A$ is intact. Here, the intrinsic loss $\kappa_E = 1-\eta-\kappa$ and the environment mode $\hat{\mathcal{E}}_E$ is in vacuum. After the nonlinear coupling, the antisqueezer, with phase compensation $-\theta_P$ on the probe, gives the final output

$$\begin{aligned}\hat{\mathcal{E}}_{P^{\rm out}} &= e^{-i\theta_P}\sqrt{G'}\hat{\mathcal{E}}_{P'} - \sqrt{G'-1}\hat{\mathcal{E}}^\dagger_A\\ &= e^{-i\theta_P}\sqrt{G'}\left(e^{i\theta_P}\sqrt{\kappa}\hat{\mathcal{E}}_P + e^{i\theta_S}\sqrt{\eta}\hat{\mathcal{E}}_S + \sqrt{\kappa_E}\hat{\mathcal{E}}_E\right) - \sqrt{G'-1}\hat{\mathcal{E}}^\dagger_A\\ &= \left(\sqrt{G\kappa G'} - \sqrt{(G'-1)(G-1)}\right)\hat{\mathcal{E}}_{P_0} + e^{i(\theta_S-\theta_P)}\sqrt{\eta G'}\hat{\mathcal{E}}_S\\ &+ \left(\sqrt{(G-1)\kappa G'} - \sqrt{(G'-1)G}\right)\hat{\mathcal{E}}^\dagger_{A_0} + e^{-i\theta_P}\sqrt{(1-\eta-\kappa)\,G'}\hat{\mathcal{E}}_E.\end{aligned} \tag{A.3}$$

To keep the output to vacuum when the input signal is vacuum, one needs to annihilate the coefficient in front of $\hat{\mathcal{E}}^\dagger_{A_0}$ in Eq. (A.3), leading to

$$G' \leftarrow G'^{\star} \equiv \frac{1}{1-\kappa+\kappa/G}. \tag{A.4}$$

By such antisqueezing, finally the output reduces to

$$\hat{\mathcal{E}}^{\star}_{P^{\rm out}} = \frac{\sqrt{\kappa}\hat{\mathcal{E}}_{P_0} + \sqrt{\eta G}e^{i(\theta_S-\theta_P)}\hat{\mathcal{E}}_S + \sqrt{(1-\eta-\kappa)G}e^{-i\theta_P}\hat{\mathcal{E}}_E}{\sqrt{G(1-\kappa)+\kappa}}. \tag{A.5}$$

Note that $\hat{\mathcal{E}}_{P_0}, \hat{\mathcal{E}}_E$ are in the vacuum state, the output can be written as

$$\hat{\mathcal{E}}^{\star}_{P^{\rm out}} = \sqrt{\eta_{\rm EA}}e^{i(\theta_S-\theta_P)}\hat{\mathcal{E}}_S + \sqrt{1-\eta_{\rm EA}}\hat{\mathcal{E}}_{\rm VAC}, \tag{A.6}$$

where the noise background $\hat{\mathcal{E}}_{\rm VAC}$ is in the vacuum state, we define the EA transduction efficiency as

$$\eta_{\rm EA} \equiv \frac{\eta G}{G(1-\kappa)+\kappa}. \tag{A.7}$$

At the same time, we can obtain the ancilla output

$$\begin{aligned}\hat{\mathcal{E}}_{A^{\rm out}} &= -e^{i\theta_P}\sqrt{G'-1}\hat{\mathcal{E}}^\dagger_{P'} + \sqrt{G'}\hat{\mathcal{E}}_A\\ &= -e^{i\theta_P}\sqrt{G'-1}\left(e^{-i\theta_P}\sqrt{\kappa}\hat{\mathcal{E}}^\dagger_P + e^{-i\theta_S}\sqrt{\eta}\hat{\mathcal{E}}^\dagger_S + \sqrt{\kappa_E}\hat{\mathcal{E}}^\dagger_E\right)\\ &+ \sqrt{G'}\hat{\mathcal{E}}_A\\ &= \left(-\sqrt{G\kappa(G'-1)} + \sqrt{G'(G-1)}\right)\hat{\mathcal{E}}^\dagger_{P_0}\\ &- e^{i(\theta_P-\theta_S)}\sqrt{\eta(G'-1)}\hat{\mathcal{E}}^\dagger_S\\ &+ \left(-\sqrt{(G-1)\kappa(G'-1)} + \sqrt{G'G}\right)\hat{\mathcal{E}}_{A_0}\\ &- e^{-i\theta_P}\sqrt{(1-\eta-\kappa)\,(G'-1)}\hat{\mathcal{E}}_E,\end{aligned} \tag{A.8}$$

$$\begin{aligned}G' \overset{\equiv}{\leftarrow} G'^{\star} = &-e^{i(\theta_P-\theta_S)}\sqrt{\eta_{\rm EA}\kappa(1-1/G)}\hat{\mathcal{E}}^\dagger_S\\ &+ (1-\kappa)\sqrt{\frac{G-1}{1-\kappa+\kappa/G}}\hat{\mathcal{E}}^\dagger_{P_0} + {\rm vac}\end{aligned} \tag{A.9}$$

where vac represents the vacuum noise terms. The ancilla output is dominated by the quantum amplification noise at the limit $G \to \infty$ with $\eta > 0$.

2. Impact of Loss in Imperfect Squeezing

Now we investigate the impact of loss in imperfect squeezers and antisqueezers. In fact, we only need to consider the loss for the ancilla after the squeezer $\mathcal{S}(G)$ and before the antisqueezer $\mathcal{S}^\dagger(G')$. This is because any loss before the squeezer does not change the vacuum state of the input ancilla and any loss after the antisqueezer does not affect the output probe (we discard the output ancilla since it is dominated by amplification noise when G is large), meanwhile any additional signal loss between squeezer and antisqueezer can be merged into the intrinsic loss κ_E, which is already included in the model of the main text. Therefore, one can also regard the squeezing-related loss as imperfect ancilla storage.

Denote the ancilla storage efficiency as κ_A (with loss $1-\kappa_A$), Eq. (A.2) becomes

$$\begin{aligned}\hat{\mathcal{E}}_{P'} &= e^{i\theta_P}\sqrt{\kappa}\hat{\mathcal{E}}_P + e^{i\theta_S}\sqrt{\eta}\hat{\mathcal{E}}_S + \sqrt{\kappa_E}\hat{\mathcal{E}}_E,\\ \hat{\mathcal{E}}_{A'} &= \sqrt{\kappa_A}\hat{\mathcal{E}}_A + \sqrt{1-\kappa_A}\hat{\mathcal{E}}_F,\end{aligned} \tag{A.10}$$

where F is the environment mode involved in the ancilla loss, initialized in the vacuum state. With the additional loss, the final output probe in Eq. (A.3) becomes

$$\begin{aligned}\hat{\mathcal{E}}_{P^{\text{out}}} &= e^{-i\theta_P}\sqrt{G'}\hat{\mathcal{E}}_{P'} - \sqrt{G'-1}\hat{\mathcal{E}}^{\dagger}_{A'}\\ &= \left(\sqrt{G\kappa G'} - \sqrt{(G'-1)(G-1)\kappa_A}\right)\hat{\mathcal{E}}_{P_0}\\ &\quad + e^{i(\theta_S-\theta_P)}\sqrt{\eta G'}\hat{\mathcal{E}}_S + \left(\sqrt{(G-1)\kappa G'} - \sqrt{(G'-1)G\kappa_A}\right)\hat{\mathcal{E}}^{\dagger}_{A_0}\\ &\quad + e^{-i\theta_P}\sqrt{(1-\eta-\kappa)\,G'}\hat{\mathcal{E}}_E - \sqrt{(G'-1)(1-\kappa_A)}\hat{\mathcal{E}}^{\dagger}_F.\end{aligned} \tag{A.11}$$

The last term invokes an additional amplification noise background, which leads to the total noise background of thermal photon number

$$N_B = \left(\sqrt{(G-1)G'\kappa} - \sqrt{(G'-1)G\kappa_A}\right)^2 + (G'-1)(1-\kappa_A) \tag{A.12}$$

as a consequence of the nonzero ancilla loss $1-\kappa_A$. In this case, the thermal noise in the output probe cannot be fully cancelled any more. The optimal choice that minimizes the output noise is

$$G'^{\star} = \frac{(G-1)\kappa_A + \sqrt{(G-1)^2\kappa_A^2 - 2(G-1)\kappa_A(G\kappa+\kappa-1) + ((G-1)\kappa+1)^2} + (G-1)\kappa + 1}{2\sqrt{2\kappa\left(G^2(-\kappa_A)+\kappa_A+G-1\right) + \left((G-1)\kappa_A+1\right)^2 + (G-1)^2\kappa^2}}. \tag{A.13}$$

We note that the additional noise, Eq. (A.12), does not increase with gain G. Thus, at the strong squeezing regime $G \gg 1$, the optimal choice of G' is similar to Eq. (6) as

$$G'^{\star} \simeq \frac{G\kappa_A}{G(\kappa_A-\kappa)+\kappa} \simeq \frac{\kappa_A}{\kappa_A-\kappa}. \tag{A.14}$$

Accordingly, the EA efficiency η_{EA} is similar to Eq. (8) as

$$\eta_{\text{EA}} = \eta G'^{\star} \simeq \eta\frac{G\kappa_A}{G(\kappa_A-\kappa)+\kappa} \simeq \eta\frac{\kappa_A}{\kappa_A-\kappa}. \tag{A.15}$$

In the presence of noise, the quantum capacity formula in Eq. (2) does not apply. Instead, we adopt a lower bound of the quantum capacity (in the units of bits) of the resulting bosonic thermal loss channel of transmissivity η_{EA} and additive thermal background photon number N_B is [65]

$$q_{\text{LB}} = \max\left\{0, \log_2\left(\frac{\eta_{\text{EA}}}{|1-\eta_{\text{EA}}|}\right) - g\left(\frac{N_B}{|1-\eta_{\text{EA}}|}\right)\right\}, \tag{A.16}$$

where $g(x) \equiv (x+1)\log_2(x+1) - x\log_2 x$.

Now we evaluate the impact of the ancilla loss on the quantum communication rate of the EA transduction. As shown in Fig. 4, the advantage of our protocol is robust to ancilla loss. The advantage survives losses as severe as $10^{-1} = 10\%$. Considering that the ancilla is not involved in the nonlinear signal–probe coupling which invokes extra losses, we expect $1-\kappa_A$ can be typically maintained lower than κ_E which is 1% here. Such robustness comes from the fact that the probe encounters loss $1-\kappa = \kappa_E + \eta$ during the nonlinear coupling process, and therefore we expect when $1-\kappa_A < \kappa_E + \eta$, the ancilla can enhance transduction as a reference with smaller loss.

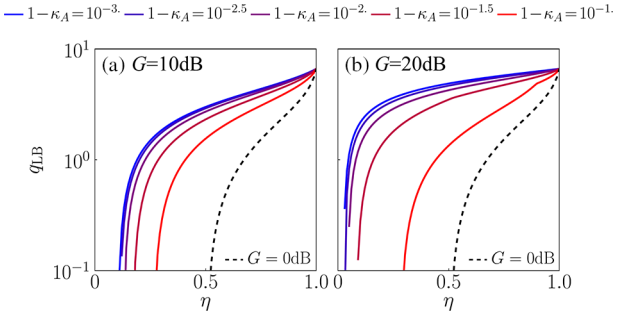

Fig. 4. Quantum capacity lower bound q_{LB} versus non-EA transduction efficiency η under various ancilla loss $1-\kappa_A$: (a) $G = 10$ dB; (b) $G = 20$ dB; black dashed, non-EA, $G = 0$ dB; intrinsic loss $\kappa_E = 0.01$.

3. Full Derivation of EBP of Electro-Optical Transduction

To solve the EBP, we make use of the integration formula

$$\int_{-\infty}^{\infty} d\omega \frac{1}{C_1 + 4\omega^2 C_2 + 16\omega^4} = \frac{\pi}{\sqrt{2}\sqrt{C_1}\sqrt{C_2+2\sqrt{C_1}}}. \tag{A.17}$$

Without the EA [see Eq. (14)], we have

$$\eta(\omega) = \frac{4C\Gamma_P^2\Gamma_S^2\zeta_P\zeta_S}{(C+1)^2\Gamma_P^2\Gamma_S^2 + 4\omega^2\left(-2C\Gamma_P\Gamma_S + \Gamma_P^2 + \Gamma_S^2\right) + 16\omega^4}. \tag{A.18}$$

With EA and optimal G' [see Eq. (8)], we have

$$\begin{aligned}&\eta_{\text{EA}}(\omega)\\ &= \frac{4C\Gamma_P^2\Gamma_S^2\zeta_P\zeta_S G}{\Gamma_P^2\Gamma_S^2\left(4(C+1)\zeta_P(G-1) + (C+1)^2 - 4\zeta_P^2(G-1)\right) + 4\omega^2}\\ &\quad\times\left(-2C\Gamma_P\Gamma_S + \Gamma_S^2 + \Gamma_P^2(4\zeta_P(\zeta_P - \zeta_P G + G - 1) + 1)\right) + 16\omega^4\end{aligned} \tag{A.19}$$

At the overcoupling limit of $\zeta_P = \zeta_S = 1$, Eq. (A.19) simplifies to

$$\eta_{\text{EA}}(0)|_{\zeta_P=\zeta_S=1} = \eta(0)\frac{G}{[1+4(G-1)C/(C+1)^2]}. \tag{A.20}$$

Now consider cooperativity $C = 4|g\alpha|^2/\Gamma_S\Gamma_P$, we fix the pump power and the nonlinear coupling coefficient, and consider EBP as a function of the cavity parameters Γ_S, Γ_P. With Eq. (A.17), we have without EA

$$\begin{aligned}\mathcal{B} &\equiv \int_{-\infty}^{\infty}\eta(\omega)d\omega = \frac{2\pi C\Gamma_P\Gamma_S\zeta_P\zeta_S}{C\Gamma_P + C\Gamma_S + \Gamma_P + \Gamma_S}\\ &= 8\pi|g\alpha|\zeta_P\zeta_S\frac{\tilde{\Gamma}_P\tilde{\Gamma}_S}{(\tilde{\Gamma}_P+\tilde{\Gamma}_S)(4+\tilde{\Gamma}_P\tilde{\Gamma}_S)},\end{aligned} \tag{A.21}$$

where we have defined $\tilde{\Gamma}_X = \Gamma_X/|g\alpha|$.

For the EA formula, we can also obtain the lengthy closed-form solution of EA EBP $\mathcal{B}_{\mathrm{EA}} \equiv \int_{-\infty}^{\infty} \eta_{\mathrm{EA}}(\omega) d\omega$ from Eq. (A.17), which we will not display here. For $\zeta_P = \zeta_S = 1$, we have a slightly simpler result,

$$\mathcal{B}_{\mathrm{EA}} = \frac{8\pi \tilde{\Gamma}_P \tilde{\Gamma}_S G|g\alpha|}{\sqrt{(\tilde{\Gamma}_P\tilde{\Gamma}_S(\tilde{\Gamma}_P\tilde{\Gamma}_S + 16G - 8) + 16)\left(\tilde{\Gamma}_P^2 + \tilde{\Gamma}_S^2 + 2\sqrt{\tilde{\Gamma}_P\tilde{\Gamma}_S(\tilde{\Gamma}_P\tilde{\Gamma}_S + 16G - 8) + 16} - 8\right)}}. \tag{A.22}$$

4. Full Model of Electro-Optical Transduction

Without loss of generality, here we take the microwave-to-optical transduction as an example, where the signal mode is at the microwave band and the probe mode is at the optical band. The cavity electro-optical dynamics based on a second-order nonlinear optical medium can be described by the Hamiltonian [15,28,29]

$$H = \hbar\omega_S \hat{a}_S^\dagger \hat{a}_S + \hbar\omega_P \hat{a}_P^\dagger \hat{a}_P - \hbar g \hat{a}_P^\dagger \hat{a}_P (\hat{a}_S + \hat{a}_S), \tag{A.23}$$

where $\hat{a}_S, \hat{a}_P$ are the annihilation operators of the signal (microwave), probe (optical), the frequencies of signal and probe are denoted as ω_S, ω_P, respectively, the nonlinear coupling coefficient is g in hertz.

Now consider a strong optical pump of mean field $\alpha e^{-i\omega_{\mathrm{pump}}t}$ with $\alpha \gg 1$, at frequency $\omega_{\mathrm{pump}} = \omega_P + \Delta$ at the red sideband (Δ<0) of the optical probe $\hat{a}_P$, then the interaction Hamiltonian becomes $-\hbar g(\hat{a}_S^\dagger + \hat{a}_S)(\hat{a}_P + \alpha e^{-i\omega_{\mathrm{pump}}t})^\dagger(\hat{a}_P + \alpha e^{-i\omega_{\mathrm{pump}}t})$. Moving $\hat{a}_P$ into the frame rotating with the optical pump, with the rotating-wave approximation the final Hamiltonian becomes

$$\hat{H} = \hbar\omega_S \hat{a}_S^\dagger \hat{a}_S - \hbar\Delta \hat{a}_P^\dagger \hat{a}_P - \hbar g(\alpha^* \hat{a}_S^\dagger \hat{a}_P + \alpha \hat{a}_S \hat{a}_P^\dagger). \tag{A.24}$$

In the main text, we considered the ideal case of $\Delta = -\omega_S$, thus one could move $\hat{a}_S$, $\hat{a}_P$ into the frame rotating with the cavity resonance frequency instead and obtain the much simpler Hamiltonian [Eq. (12)].

The input–output relation is described by the Langevin equation [71,75]. Below, we summarize the solution of Langevin equation for cavity electro-optical transduction [28,29].

a. Input–Output Relation

Consider input field operator vector $\hat{\boldsymbol{\mathcal{E}}}_{in} \equiv [\hat{\mathcal{E}}_{S,in}, \hat{\mathcal{E}}_{S,E}, \hat{\mathcal{E}}_{P,in}, \hat{\mathcal{E}}_{P,E}, \hat{\mathcal{E}}_{S,in}^\dagger, \hat{\mathcal{E}}_{S,E}^\dagger, \hat{\mathcal{E}}_{P,in}^\dagger, \hat{\mathcal{E}}_{P,E}^\dagger]^T$, where $\hat{\mathcal{E}}_{S,in}, \hat{\mathcal{E}}_{P,in}$ are input fields at signal and probe frequencies, respectively, $\hat{\mathcal{E}}_{S,E}, \hat{\mathcal{E}}_{P,E}$ are environment fields at signal and probe frequencies, respectively; and similarly output field operator vector $\hat{\boldsymbol{\mathcal{E}}}_{out} \equiv [\hat{\mathcal{E}}_{S,out}, \hat{\mathcal{E}}_{P,out}, \hat{\mathcal{E}}_{S,out}^\dagger, \hat{\mathcal{E}}_{P,out}^\dagger]^T$; also the cavity mode annihilation operator vector $\hat{\boldsymbol{a}} \equiv [\hat{a}_S, \hat{a}_P, \hat{a}_S^\dagger, \hat{a}_P^\dagger]^T$. With the strong optical pump, the Langevin equation is linearized as

$$\frac{d}{dt}\hat{\boldsymbol{a}}(t) = A\hat{\boldsymbol{a}}(t) + B\hat{\boldsymbol{\mathcal{E}}}_{in}(t), \quad \hat{\boldsymbol{\mathcal{E}}}_{out}(t) = C\hat{\boldsymbol{a}}(t) + D\hat{\boldsymbol{\mathcal{E}}}_{in}(t), \tag{A.25}$$

where

$$A = \begin{pmatrix} -\frac{\Gamma_S}{2} - i\Delta_S & ig\alpha & 0 & 0 \\ ig\alpha & -\frac{\Gamma_P}{2} + i\Delta_P & 0 & 0 \\ 0 & 0 & -\frac{\Gamma_S}{2} + i\Delta_S & -ig\alpha^* \\ 0 & 0 & -ig\alpha^* & -\frac{\Gamma_P}{2} - i\Delta_P \end{pmatrix},$$

$$B = \begin{pmatrix} \sqrt{\gamma_{S,c}} & \sqrt{\gamma_{S,0}} & 0 & 0 & 0 & 0 & 0 & 0 \\ 0 & 0 & \sqrt{\gamma_{P,c}} & \sqrt{\gamma_{P,0}} & 0 & 0 & 0 & 0 \\ 0 & 0 & 0 & 0 & \sqrt{\gamma_{S,c}} & \sqrt{\gamma_{S,0}} & 0 & 0 \\ 0 & 0 & 0 & 0 & 0 & 0 & \sqrt{\gamma_{P,c}} & \sqrt{\gamma_{P,0}} \end{pmatrix},$$

$$C = \begin{pmatrix} \sqrt{\gamma_{S,c}} & 0 & 0 & 0 \\ 0 & \sqrt{\gamma_{P,c}} & 0 & 0 \\ 0 & 0 & \sqrt{\gamma_{S,c}} & 0 \\ 0 & 0 & 0 & \sqrt{\gamma_{P,c}} \end{pmatrix},$$

$$D = \begin{pmatrix} -1 & 0 & 0 & 0 & 0 & 0 & 0 & 0 \\ 0 & 0 & -1 & 0 & 0 & 0 & 0 & 0 \\ 0 & 0 & 0 & 0 & -1 & 0 & 0 & 0 \\ 0 & 0 & 0 & 0 & 0 & 0 & -1 & 0 \end{pmatrix}, \tag{A.26}$$

where $\gamma_{S,0}, \gamma_{S,c}$ are the intrinsic loss rate and the coupling rate of the signal cavity, similar for $\gamma_{P,0}, \gamma_{P,c}$ of the probe cavity, and $\Gamma_S = \gamma_{S,0} + \gamma_{S,c}, \Gamma_P = \gamma_{P,0} + \gamma_{P,c}$ are total linewidths. We define the coupling ratios $\zeta_P \equiv \gamma_{P,c}/\Gamma_P, \zeta_S \equiv \gamma_{S,c}/\Gamma_S$. In the steady-state limit, it is convenient to consider the frequency spectrum of the input–output relation. Fourier transform of the Langevin equation gives

$$\hat{\boldsymbol{\mathcal{E}}}_{out}(\omega) = S(\omega)\hat{\boldsymbol{\mathcal{E}}}_{in}(\omega), \tag{A.27}$$

where ω is the frequency at the frame rotating with the pump frequency for the optical probe (stationary frame for the microwave signal), the spectral transfer matrix $S(\omega) = C(-i\omega I_4 - A)^{-1}B + D$, I_4 is a 4×4 identity matrix. Note that here ω is in a different rotating frame from that in main text. From Eq. (A.36), we obtain the cavity transmissivity for the optical probe

$$\kappa_{\mathrm{oo}}(\omega) = |S_{23}(\omega)|^2 = \frac{C^2\Gamma_P^2\Gamma_S^2 - 2C\Gamma_P\Gamma_S\left(\Gamma_P\left(2\zeta_P - 1\right)\Gamma_S + 4\left(\omega - \omega_S\right)\left(\Delta_P + \omega\right)\right) + \left(\Gamma_S^2 + 4\left(\omega - \omega_S\right)^2\right)\left(\Gamma_P^2\left(1 - 2\zeta_P\right)^2 + 4\left(\Delta_P + \omega\right)^2\right)}{\Gamma_P^2\Gamma_S^2\left|C + \left(1 - \frac{2i(\omega+\Delta_P)}{\Gamma_P}\right)\left(\frac{2i(\omega_S-\omega)}{\Gamma_S} + 1\right)\right|^2}, \tag{A.28}$$

and the intrinsic conversion efficiency of electro-optical transduction

$$\eta_{\mathrm{eo}}(\omega) = |S_{13}(\omega)|^2 = \frac{4C\zeta_P\zeta_S}{\left|C + \left(1 - \frac{2i(\omega+\Delta_P)}{\Gamma_P}\right)\left(\frac{2i(\omega_S-\omega)}{\Gamma_S} + 1\right)\right|^2}, \tag{A.29}$$

which agree with Eq. (13) and Eq. (14) with $\Delta \to -\omega_S$, $\omega \to \omega + \omega_S$. Below, we evaluate the impact of the pump detuning imperfection $\delta \equiv \Delta + \omega_S$ from the ideal detuning $-\omega_S$.

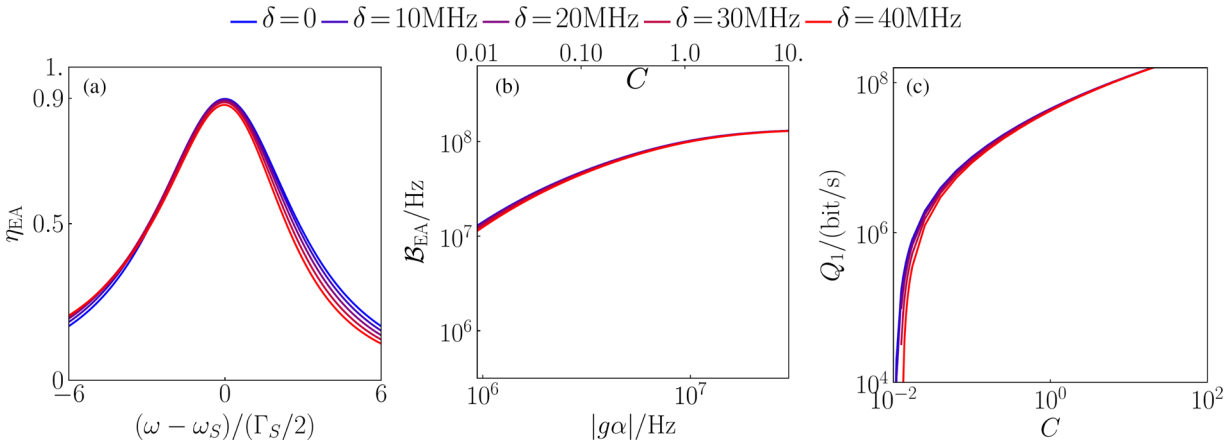

Fig. 5. Figure 3 with pump detuned from the probe cavity resonance frequency by various $\Delta = \omega_{\text{pump}} - \omega_P = -\omega_S + \delta$, where δ is the detuning imperfection from the ideal detuning $-\omega_S$. We consider δ ranging from 0 to 40 MHz ($\simeq 3\Gamma_S$). Here the squeezer gain is fixed to $G = 30$ dB. (a) The EA transduction efficiency spectrum $\eta_{\text{EA}}(\omega)$ under various δ. $C = 0.1$. (b) The EA EBP $\mathcal{B}_{\text{EA}}$ versus the effective nonlinear coupling strength $|g\alpha|$. We fix Γ_P, Γ_S, for which we provide the cooperativity C values as the upper axis ticks. (c) Broadband quantum capacity rate Q_1 versus cooperativity C. In all figures, $\zeta_P = \zeta_S = 0.99$; linewidths $\Gamma_P = 25.8$ MHz, $\Gamma_S = 13.706$ MHz are chosen according to the high-cooperativity setup in Ref. [29].

b. Evaluation of the Impact of Imperfect Pump Detunings

Figure 5 shows the impact on Fig. 3 when the pump detuning $\Delta = \omega_{\text{pump}} - \omega_P$ deviates from the ideal value $-\omega_S$ by an imperfection δ. We plot δ ranging from 0 to 40 MHz ($\simeq 3B$), where $B \approx \Gamma_S = 13.706$ MHz is the bandwidth of the cavity electro-optical coupler. In Fig. 5(a), we see a decay in the EA efficiency η_{EA} with increasing δ, but at a negligible level. Such robustness against detuning imperfection δ is because the intrinsic loss spectrum $\kappa_E(\omega) = 1 - \kappa(\omega) - \eta(\omega)$ is centered around the probe cavity resonance frequency $\omega = -\Delta$ (ω is in the frame rotating with pump) while the electro-optic conversion efficiency spectrum $\eta(\omega)$ is always centered around $\omega = \omega_S$ due to energy conservation, thus the high efficiency region enjoys a smaller κ_E for larger detuning imperfection $|\delta|$, and our EA protocol benefits from small κ_E as shown in Eq. (11). Such robustness of EA efficiency spectrum $\eta_{\text{EA}}(\omega)$ immediately leads to similar robustness of the EA EBP and quantum capacity, as shown in Figs. 5(b) and 5(c).

5. Implementation of Frequency-Dependent Antisqueezer

Here we present a simple design of the frequency-dependent antisqueezer to beat the quantum capacity of the non-EA transduction.

We aim to approach the noiseless antisqueezing gain spectrum $G'^{\star}(\omega)$ according to Eq. (6). Ideally, $G'^{\star}(\omega) \propto 1/\eta(\omega)$ according to Eq. (10) at $G \to \infty$, which is approximately the inverse of the quasi-Lorentzian cavity lineshape $\eta(\omega)$. We propose to adopt a sequential array of cavities to approximate the required spectrum. Here, we consider a specific setup of a two-periodic array—alternating antisqueezers and squeezers—as shown in Fig. 6. We consider a specific class of parametric amplifiers (PAs) of given lineshape as squeezers (and antisqueezers up to π phase) with tunable gains and linewidths, and concatenate the squeezers and antisqueezers of various gains and linewidths sequentially together, to approach the desired squeezing lineshape $G'^{\star}(\omega)$.

We investigate a specific class of doubly resonant cavity PA [82] as an example, which is subject to the Heisenberg–Langevin equations $\frac{d}{dt}\hat{a}_{S_i} = -\Gamma_i \hat{a}_{S_i} + g_i\Gamma_i \hat{a}^{\dagger}_{I_i} + \sqrt{2\Gamma_i}\hat{a}_{S_i,in}$, $\frac{d}{dt}\hat{a}_{I_i} = -\Gamma_i \hat{a}_{I_i} + g_i\Gamma_i \hat{a}^{\dagger}_{S_i} + \sqrt{2\Gamma_i}\hat{a}_{I_i,in}$ for signal mode S_i and idler mode I_i resonant at the same frequency, where g_i, Γ_i are the normalized gain (the ratio of pump power over threshold power) and half-linewidth for the ith PA. The squeezing gain lineshape is then

$$G_i(\omega) = 1 + \frac{4g_i^2}{\left(-g_i^2 - \frac{\omega^2}{\Gamma_i^2} + 1\right)^2 + \frac{4\omega^2}{\Gamma_i^2}}. \tag{A.30}$$

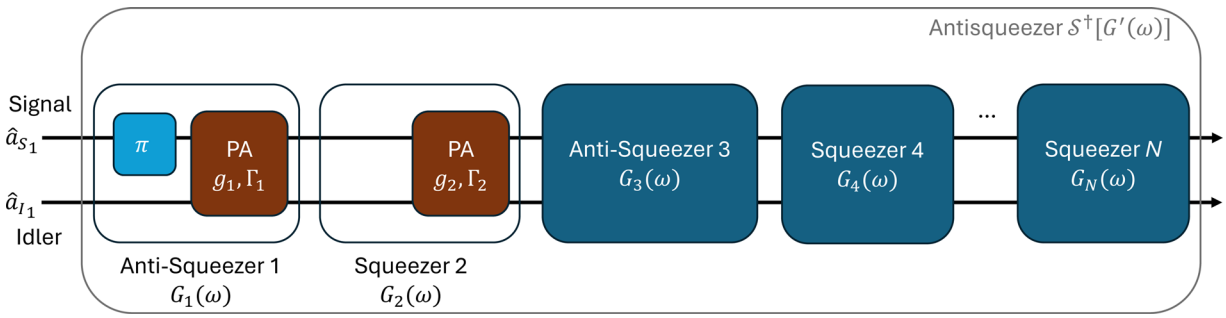

Fig. 6. Schematic of the design of frequency-dependent antisqueezer using N-layer two-periodic sequential PA array with individually tunable gain spectrum $G_i(\omega)$'s determined by normalized gain g_i's and linewidth Γ_i's, $i = 1, 2, \ldots, N$. Each squeezer component is implemented by a PA, while each antisqueezer component consists of the same type of PA with a π phase shift on either signal or idler input port.

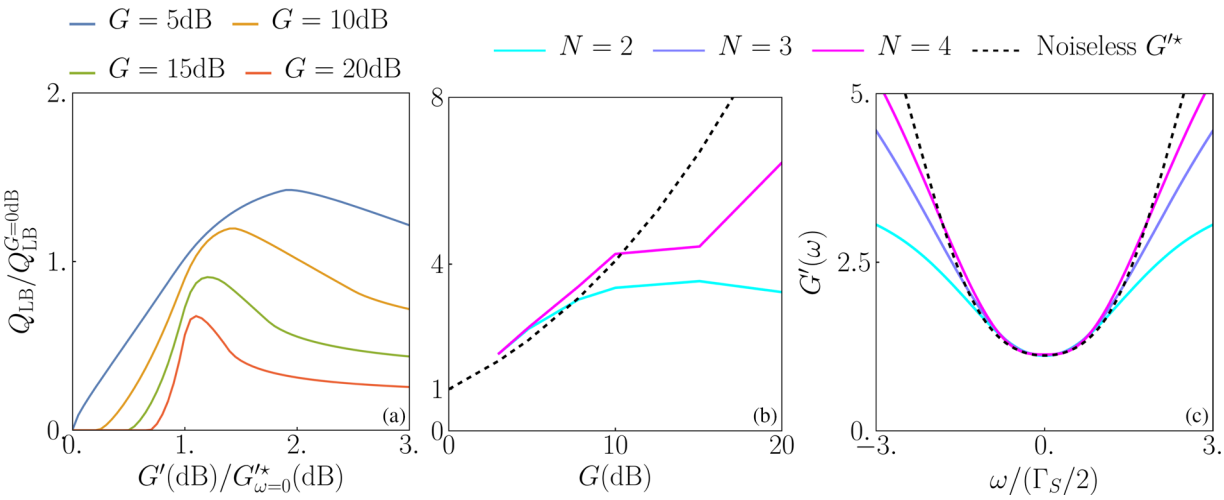

Fig. 7. Performance of various designs of antisqueezer. (a) Control group, EA advantage of an ultra-broadband antisqueezer of constant gain $G'(\omega) = G'$ in Q_{LB} [Eq. (A.32)] over non-EA $Q_{\mathrm{LB}}^{G=0\mathrm{dB}}$, the x axis is normalized by the on-resonance noiseless antisqueezing gain $G'^{\star}_{\omega=0} = \frac{1}{1-\kappa(\omega=0)+\kappa(\omega=0)/G}$ (in decibel units); (b) EA advantage of frequency-dependent antisqueezer using N-layer two-periodic sequential PA array (see Fig. 6) with numerically optimized g_i's and Γ_i's, compared with the advantage using noiseless antisqueezing $G'^{\star}$ (black dashed) which can be surpassed for $G \leq 10$ dB, since η_{EA} can be further increased at the cost of increasing noise; (c) the overall antisqueezing gain spectrum $G'(\omega)$ achieved by the N-layer sequential PA arrays, under fixed input squeezing $G = 10$ dB, compared with the noiseless antisqueezing gain spectrum $G'^{\star}(\omega)$ (black dashed). In all panels, $\kappa(\omega), \eta(\omega)$ are calculated using the parameter setup $\Gamma_P = 25.8$ MHz, $\Gamma_S = 13.706$ MHz, chosen from the high-cooperativity setup in Ref. [29]. Here we consider ideally overcoupled cavities $\zeta_P = \zeta_S = 1$ to accelerate the numerical simulation; and $C = 0.49$, higher than $C = 0.1$ in the main text, since the EA advantage is always infinite as $Q_{\mathrm{LB}}^{G=0\mathrm{dB}} = 0$ in the latter case.

It is trivial to derive the overall gain for the N-layer sequential array iteratively, while the general formula of any N is too lengthy to be presented here. Note that the overall gain is not simply the multiplication of individual gains, due to the interferences with the idler. For $N = 2$, the overall gain $G'(\omega) = \left(\sqrt{(G_1(\omega)-1)(G_2(\omega)-1)} - \sqrt{G_1(\omega)G_2(\omega)}\right)^2$.

An imperfect antisqueezer gain G' invokes additional thermal background of mean photon number

$$N_B(\omega) = \left(\sqrt{G\,(G'(\omega)-1)} \mp \sqrt{(G-1)\kappa(\omega)G'(\omega)}\right)^2, \quad \textbf{(A.31)}$$

where $\mp$ is $-$ for an antisqueezer or $+$ for a squeezer. For $G'(\omega) \to 1, \kappa(\omega) \to 1$, it reduces to the well-known quantum-limited phase-insensitive linear amplification noise $G-1$ [36,69].

A lower bound of the broadband quantum capacity rate of the resulting bosonic thermal loss channel of transmissivity η_{EA} and additive thermal background photon number N_B has been presented as Eq. (A.16) in Appendix A, Section 2. The broadband rate of it is

$$Q_{\mathrm{LB}} = \int_{-\infty}^{\infty} \max\left\{0, \log_2\left(\frac{\eta_{\mathrm{EA}}(\omega)}{|1-\eta_{\mathrm{EA}}(\omega)|}\right) - g\left(\frac{N_B(\omega)}{|1-\eta_{\mathrm{EA}}(\omega)|}\right)\right\}\frac{d\omega}{2\pi}, \quad \textbf{(A.32)}$$

which is in units of bits per seconds. We use this lower bound to benchmark the performance of our frequency-dependent antisqueezer designs using the sequential PA array.

In Fig. 7, we evaluate the performance of the protocol.

We begin with a control group, a simple ultra-broadband antisqueezer of uniform gain spectrum, to provide a baseline of the advantage of our proposal of the sequential PA array. Figure 7(a) plots the EA advantage in quantum capacity over the non-EA case, with the uniform antisqueezer of constant gain G'. We find that the optimal choice of G' close to the noiseless on-resonance value $G'^{\star}_{\omega=0}$ as expected. However, the EA advantage is limited to <2. In fact, the advantage degrades as the input squeezing G increases from 5 dB (blue) to 20 dB (red). For $G \geq 15$ dB, the EA protocol with such uniform antisqueezer cannot even beat the non-EA case. This is because the quantum amplification noise $N_B(\omega)$ grows with the mismatching between G' and the noiseless gain $G'^{\star}(\omega)$ [Eq. (6)] more rapidly as G increases, as shown in Eq. (A.31).

Next, we numerically optimize the normalized gain g_i's and linewidth Γ_i's of the PAs to maximize the quantum capacity lower bound of Eq. (A.32). In Fig. 7(b), we observe that the advantage bottleneck due to antisqueezing mismatching is resolved by our sequential PA. Now the EA advantage increases with G. With $N = 4$, a factor of 6.44 advantage is achieved at $G = 20$ dB. Further increasing the layer number N may continue to boost the advantage, while the numerical optimization is too costly and we leave it for future study. Remarkably, we observe that the noiseless performance can be surpassed by our sequential PA antisqueezer for $G \leq 10$ dB, this is not surprising since the EA efficiency $\eta_{\mathrm{EA}}(\omega)$ can always be further increased by larger $G'(\omega)$ at the cost of increasing noise $N_B(\omega)$ (which increases with G), note that data processing inequality does not apply here because overamplifying (over-antisqueezing) is not a simple Gaussian amplification channel here with the entanglement assistance. In Fig. 7(c), we verify that, with increasing layer number N, the optimized overall antisqueezing gain spectrum indeed approaches the inverse-Lorentzian shape $G'^{\star}(\omega) \propto 1/\eta(\omega)$ as expected.

6. Electro-Optomechanical Transduction

The cavity electro-optomechanical dynamics can be described by the full Hamiltonian [11,75]

$$H = \hbar\omega_S \hat{a}_S^{\dagger}\hat{a}_S + \hbar\omega_P \hat{a}_P^{\dagger}\hat{a}_P + \hbar\omega_M \hat{a}_M^{\dagger}\hat{a}_M - \hbar g_S \hat{a}_S^{\dagger}\hat{a}_S\hat{x}_M - \hbar g_P \hat{a}_P^{\dagger}\hat{a}_P\hat{x}_M, \quad \textbf{(A.33)}$$

where $\hat{a}_S, \hat{a}_P, \hat{a}_M$ are the annihilation operators of the signal (microwave), probe (optical), and mediating (mechanical) modes, $\hat{x}_M = x_{\mathrm{zp}}(\hat{a}_M + \hat{a}_M^\dagger)$ with $x_{\mathrm{zp}} = \sqrt{\frac{\hbar}{2m\omega_M}}$, the frequencies of signal, probe, and mediating modes are denoted as ω_S, ω_P, and ω_M. Here the nonlinear coupling coefficients g_S, g_P (of electro-mechanical and optomechanical couplings, respectively) are in units of hertz per meter. (In the brackets we take the microwave-to-optical transduction as an example.) We define $\mathcal{G}_{S,P} \equiv g_{S,P} x_{\mathrm{zp}} \alpha_{S,P}$ proportional to the nonlinear coupling coefficients and the pumping amplitudes, analogous to $g\alpha$ in the electro-optical coupling [16]. Without loss of generality, we assume $\mathcal{G}_{S,P}$ real.

The input–output relation is described by the Langevin equation [71,75]. Below we summarize the solution of Langevin equation for cavity electro-optomechanical transduction [11].

a. Input–Output Relation

Consider input field operator vector $\hat{\boldsymbol{\mathcal{E}}}_{in} \equiv [\hat{\mathcal{E}}_{S,in}, \hat{\mathcal{E}}_{S,E}, \hat{\mathcal{E}}_{P,in}, \hat{\mathcal{E}}_{P,E}, \hat{\mathcal{E}}_{M,E}, \hat{\mathcal{E}}_{S,in}^\dagger, \hat{\mathcal{E}}_{S,E}^\dagger, \hat{\mathcal{E}}_{P,in}^\dagger, \hat{\mathcal{E}}_{P,E}^\dagger, \hat{\mathcal{E}}_{M,E}^\dagger]^T$, where $\hat{\mathcal{E}}_{S,in}, \hat{\mathcal{E}}_{P,in}$ are input fields at signal and probe frequencies, respectively, $\hat{\mathcal{E}}_{S,E}, \hat{\mathcal{E}}_{P,E}, \hat{\mathcal{E}}_{M,E}$ are environment fields at signal, probe, and mediating frequencies, respectively; and similarly output field operator vector $\hat{\boldsymbol{\mathcal{E}}}_{out} \equiv [\hat{\mathcal{E}}_{S,out}, \hat{\mathcal{E}}_{P,out}, \hat{\mathcal{E}}_{S,out}^\dagger, \hat{\mathcal{E}}_{P,out}^\dagger]^T$; also the cavity mode annihilation operator vector $\hat{\boldsymbol{a}} \equiv [\hat{a}_S, \hat{a}_P, \hat{a}_M, \hat{a}_S^\dagger, \hat{a}_P^\dagger, \hat{a}_M^\dagger]^T$. With strong pumps, the Langevin equation is linearized as

$$\frac{d}{dt}\hat{\boldsymbol{a}}(t) = A\hat{\boldsymbol{a}}(t) + B\hat{\boldsymbol{\mathcal{E}}}_{in}(t), \quad \hat{\boldsymbol{\mathcal{E}}}_{out}(t) = C\hat{\boldsymbol{a}}(t) + D\hat{\boldsymbol{\mathcal{E}}}_{in}(t), \tag{A.34}$$

where

$$A = \begin{pmatrix} -\frac{\Gamma_S}{2} + i\Delta_S & 0 & i\mathcal{G}_S & 0 & 0 & i\mathcal{G}_S \\ 0 & -\frac{\Gamma_P}{2} + i\Delta_P & i\mathcal{G}_P & 0 & 0 & i\mathcal{G}_P \\ i\mathcal{G}_S & i\mathcal{G}_P & -\frac{\Gamma_M}{2} - i\omega_M & i\mathcal{G}_S & i\mathcal{G}_P & 0 \\ 0 & 0 & -i\mathcal{G}_S & -\frac{\Gamma_S}{2} - i\Delta_S & 0 & -i\mathcal{G}_S \\ 0 & 0 & -i\mathcal{G}_P & 0 & -\frac{\Gamma_P}{2} - i\Delta_P & -i\mathcal{G}_P \\ -i\mathcal{G}_S & -i\mathcal{G}_P & 0 & -i\mathcal{G}_S & -i\mathcal{G}_P & -\frac{\Gamma_M}{2} + i\omega_M \end{pmatrix}, \tag{A.35}$$

$$B = \begin{pmatrix} \sqrt{\gamma_{S,c}} & \sqrt{\gamma_{S,0}} & 0 & 0 & 0 & 0 & 0 & 0 & 0 & 0 \\ 0 & 0 & \sqrt{\gamma_{P,c}} & \sqrt{\gamma_{P,0}} & 0 & 0 & 0 & 0 & 0 & 0 \\ 0 & 0 & 0 & 0 & \sqrt{\Gamma_M} & 0 & 0 & 0 & 0 & 0 \\ 0 & 0 & 0 & 0 & 0 & \sqrt{\gamma_{S,c}} & \sqrt{\gamma_{S,0}} & 0 & 0 & 0 \\ 0 & 0 & 0 & 0 & 0 & 0 & 0 & \sqrt{\gamma_{P,c}} & \sqrt{\gamma_{P,0}} & 0 \\ 0 & 0 & 0 & 0 & 0 & 0 & 0 & 0 & 0 & \sqrt{\Gamma_M} \end{pmatrix},$$

$$C = \begin{pmatrix} \sqrt{\gamma_{S,c}} & 0 & 0 & 0 & 0 & 0 \\ 0 & \sqrt{\gamma_{P,c}} & 0 & 0 & 0 & 0 \\ 0 & 0 & 0 & \sqrt{\gamma_{S,c}} & 0 & 0 \\ 0 & 0 & 0 & 0 & \sqrt{\gamma_{P,c}} & 0 \end{pmatrix}, \quad D = \begin{pmatrix} -1 & 0 & 0 & 0 & 0 & 0 & 0 & 0 & 0 & 0 \\ 0 & 0 & -1 & 0 & 0 & 0 & 0 & 0 & 0 & 0 \\ 0 & 0 & 0 & 0 & 0 & -1 & 0 & 0 & 0 & 0 \\ 0 & 0 & 0 & 0 & 0 & 0 & 0 & -1 & 0 & 0 \end{pmatrix},$$

where $\gamma_{S,0}, \gamma_{S,c}$ are the intrinsic loss rate and the coupling rate of the signal cavity, similar for $\gamma_{P,0}, \gamma_{P,c}$ of the probe cavity, total linewidth $\Gamma_S = \gamma_{S,0} + \gamma_{S,c}, \Gamma_P = \gamma_{P,0} + \gamma_{P,c}$, Δ_S, Δ_P are the detunings of the pumps from the resonance frequencies for signal and probe cavities, respectively. We define the coupling ratios $\zeta_P \equiv \gamma_{P,c}/\Gamma_P, \zeta_S \equiv \gamma_{S,c}/\Gamma_S$. In the steady-state limit, it is convenient to consider the frequency spectrum of the input–output relation. Fourier transform of the Langevin equation gives

$$\hat{\boldsymbol{\mathcal{E}}}_{out}(\omega) = S(\omega)\hat{\boldsymbol{\mathcal{E}}}_{in}(\omega) \tag{A.36}$$

where ω is the frequency at the frame rotating with the pump frequencies of signal and probe (stationary frame for the mediating mode), the spectral transfer matrix $S(\omega) = C(-i\omega I_6 - A)^{-1}B + D$, I_6 is a 6×6 identity matrix. Note that here ω is in a different rotating frame from the electro-optics model in main text.

Now consider the red sideband detuning $\Delta_S = \Delta_P = -\omega_M$ to maximize the noiseless beam-splitter-type conversion and suppress the noisy blue sideband squeezing-type conversion [30,61]. From Eq. (A.36), we obtain the intrinsic conversion efficiency of electro-optomechanical transduction at the frequency resolved limit $\Gamma_S, \Gamma_P \ll \omega_M$,

$$\begin{aligned} &\eta_{\mathrm{emo}}(\omega) \\ &\quad \equiv |S_{13}(\omega)|^2\Big|_{\Delta_S=\Delta_P=-\omega_M;\Gamma_S,\Gamma_P\ll\omega_M} \\ &\quad = \frac{64\mathcal{G}_P{}^2\mathcal{G}_S{}^2\Gamma_P\zeta_P\Gamma_S\zeta_S}{4\Delta\omega^2\left(4\mathcal{G}_P{}^2 + 4\mathcal{G}_S{}^2 + \Gamma_M\Gamma_P + \Gamma_M\Gamma_S + \Gamma_P\Gamma_S - 4\Delta\omega^2\right)^2} \\ &\qquad + \left(4\mathcal{G}_S{}^2\Gamma_P + 4\mathcal{G}_P{}^2\Gamma_S - 4\Delta\omega^2\left(\Gamma_M + \Gamma_P + \Gamma_S\right) + \Gamma_M\Gamma_P\Gamma_S\right)^2 \end{aligned} \tag{A.37}$$

where $\Delta\omega \equiv \omega - \omega_M$.

b. The EBP

The transduction efficiency, Eq. (A.37), has six pure imaginary poles in three pairs $p_1, p_2, p_3, p_4 = -p_1, p_5 = -p_2, p_6 = -p_3$, of which the formulas are too lengthy to be shown here. Thus, the

spectral integral gives the EBP

$$\mathcal{B}^{\text{emo}} \equiv \int_{-\infty}^{\infty} \eta_{\text{emo}}(\omega) d\omega = \frac{i\pi\,(p_1+p_2+p_3)\,\mathcal{G}_P{}^2\mathcal{G}_S{}^2\Gamma_P\Gamma_S\zeta_P\zeta_S}{(p_1+p_2)\,(p_1+p_3)\,(p_2+p_3)\,p_1p_2p_3}. \tag{A.38}$$

Here $\mathcal{B}^{\text{emo}}$ is always real as the imaginary sign in the numerator cancels with the imaginary signs of the poles. We find that $\mathcal{B}^{\text{emo}}$ is maximized at $\Gamma_M \to 0$, given finite cooperativity $C_S = 4\mathcal{G}_S{}^2/\Gamma_S\Gamma_m$, $C_P = 4\mathcal{G}_P{}^2/\Gamma_P\Gamma_m$. In this case, $p_1 \simeq i\frac{\Gamma_M(C_P+C_S+1)}{2}$, $p_2 \simeq \frac{i\Gamma_P}{2}$, $p_3 \simeq \frac{i\Gamma_S}{2}$, which gives

$$\mathcal{B}^{\text{emo}}|_{\Gamma_M\to 0} \simeq \frac{8\pi\mathcal{G}_P{}^2\mathcal{G}_S{}^2\Gamma_P^2\zeta_P\Gamma_S^2\zeta_S\left(4\mathcal{G}_P{}^2\Gamma_S + 4\mathcal{G}_S{}^2\Gamma_P + \Gamma_P\Gamma_S\left(\Gamma_P+\Gamma_S\right)\right)}{\left(\Gamma_P+\Gamma_S\right)\left(\mathcal{G}_P{}^2\Gamma_S + \mathcal{G}_S{}^2\Gamma_P\right)\left(4\mathcal{G}_P{}^2\Gamma_S + \Gamma_P\left(4\mathcal{G}_S{}^2 + \Gamma_P\Gamma_S\right)\right)\left(4\mathcal{G}_P{}^2\Gamma_S + \Gamma_P\left(4\mathcal{G}_S{}^2 + \Gamma_S^2\right)\right)}. \tag{A.39}$$

In the symmetric case of $\mathcal{G}_P = \mathcal{G}_S = \mathcal{G}$, we can obtain the maximum analytically

$$\mathcal{B}^{\text{emo}}_{\max} = \frac{\sqrt{107+51\sqrt{17}}}{32}\pi\zeta_P\zeta_S\mathcal{G} \simeq 1.749\zeta_P\zeta_S\mathcal{G}. \tag{A.40}$$

In the general case of $\mathcal{G}_P \neq \mathcal{G}_S$, exact maximization is in general challenging. By eliminating terms in the denominator, we find the EBP is upper-bounded by

$$\mathcal{B}^{\text{emo}}|_{\Gamma_M\to 0} \le \pi\zeta_P\zeta_S\left[4\mathcal{G}_P{}^2\Gamma_S + 4\mathcal{G}_S{}^2\Gamma_P + \Gamma_P\Gamma_S\left(\Gamma_P+\Gamma_S\right)\right] \cdot \min\left\{\frac{\mathcal{G}_S{}^2\Gamma_P^2}{2\mathcal{G}_P{}^4\Gamma_S^2}, \frac{\mathcal{G}_P{}^2\Gamma_S^2}{2\mathcal{G}_S{}^4\Gamma_P^2}, \frac{8\mathcal{G}_S{}^2}{\Gamma_S^3\Gamma_P}\right\} \equiv \mathcal{B}^{\text{emo}}_{\text{UB}}, \tag{A.41}$$

which is maximized to a finite value over any cavity linewidth Γ_S, Γ_P

$$\mathcal{B}^{\text{emo}}_{\text{UB,max}} = \frac{4\pi\sqrt[8]{\mathcal{G}_P}\zeta_P\zeta_S\left(\left(\mathcal{G}_P\mathcal{G}_S\right)^{3/4} + \sqrt[4]{\mathcal{G}_P\mathcal{G}_S{}^5} + \mathcal{G}_P{}^{3/2} + \mathcal{G}_S{}^{3/2}\right)}{\mathcal{G}_S{}^{5/8}} \tag{A.42}$$

at $\Gamma_S \to \frac{2\mathcal{G}_S{}^{9/8}}{\sqrt[8]{\mathcal{G}_P}}$, $\Gamma_P \to \frac{2\mathcal{G}_P{}^{11/8}}{\mathcal{G}_S{}^{3/8}}$, where the coupling ratios $\zeta_P, \zeta_S \le 1$. As a reminder, here $\mathcal{G}_P, \mathcal{G}_S$ are analogous to $|g\alpha|$ of electro-optical coupling which are independent on cavity quality factor or coupling rate. Hence, similar to the electro-optical transducers, the EBP of electro-optomechanical transducers is fundamentally limited regardless of any cavity engineering.

We note that our result of $\mathcal{B}^{\text{emo}}_{\text{UB,max}}$ is not symmetric about S, P since we arbitrarily chose the terms in the denominator of $\mathcal{B}^{\text{emo}}|_{\Gamma_M\to 0}$ to eliminate, which leads to a loose upper bound $\mathcal{B}^{\text{emo}}_{\text{UB}}$. More careful choices are likely to offer a tighter upper bound.

Funding. National Science Foundation (OMA-2326746, CCF-2240641, 1941583); Defense Advanced Research Projects Agency (HR0011-24-9-0362); Office of Naval Research (N00014-23-1-2296); Google; Office of Science (DE-AC02-07CH11359).

Acknowledgments. H.S. and Q.Z. proposed the protocol in discussion, performed the analyses, generated the figures, and wrote the manuscript.

Disclosures. The authors declare no conflicts of interest.

Data availability. The data supporting the findings of this study are available from the first author (H.S.) upon reasonable request.

REFERENCES

1. N. Lauk, N. Sinclair, S. Barzanjeh, *et al.*, "Perspectives on quantum transduction," Quantum Sci. Technol. **5**, 020501 (2020).
2. D. Awschalom, K. K. Berggren, H. Bernien, *et al.*, "Development of quantum interconnects (QuICs) for next-generation information technologies," PRX Quantum **2**, 017002 (2021).
3. X. Han, W. Fu, C.-L. Zou, *et al.*, "Microwave-optical quantum frequency conversion," Optica **8**, 1050–1064 (2021).
4. A. Acín, J. I. Cirac, and M. Lewenstein, "Entanglement percolation in quantum networks," Nat. Phys. **3**, 256–259 (2007).
5. H. J. Kimble, "The quantum internet," Nature **453**, 1023–1030 (2008).
6. S. Wehner, D. Elkouss, and R. Hanson, "Quantum internet: A vision for the road ahead," Science **362**, 6412 (2018).
7. W. Kozlowski and S. Wehner, "Towards large-scale quantum networks," in *Proceedings of the Sixth Annual ACM International Conference on Nanoscale Computing and Communication* (2019), pp. 1–7.
8. Z. Zhang and Q. Zhuang, "Distributed quantum sensing," Quantum Sci. Technol. **6**, 043001 (2021).
9. C. Monroe, R. Raussendorf, A. Ruthven, *et al.*, "Large-scale modular quantum-computer architecture with atomic memory and photonic interconnects," Phys. Rev. A **89**, 022317 (2014).
10. S. Barz, E. Kashefi, A. Broadbent, *et al.*, "Demonstration of blind quantum computing," Science **335**, 303–308 (2012).
11. R. W. Andrews, R. W. Peterson, T. P. Purdy, *et al.*, "Bidirectional and efficient conversion between microwave and optical light," Nat. Phys. **10**, 321–326 (2014).
12. J. Bochmann, A. Vainsencher, D. D. Awschalom, *et al.*, "Nanomechanical coupling between microwave and optical photons," Nat. Phys. **9**, 712–716 (2013).
13. A. Vainsencher, K. Satzinger, G. Peairs, *et al.*, "Bi-directional conversion between microwave and optical frequencies in a piezoelectric optomechanical device," Appl. Phys. Lett. **109**, 033107 (2016).
14. K. C. Balram, M. I. Davanço, J. D. Song, *et al.*, "Coherent coupling between radiofrequency, optical and acoustic waves in piezo-optomechanical circuits," Nat. Photonics **10**, 346–352 (2016).
15. M. Tsang, "Cavity quantum electro-optics," Phys. Rev. A **81**, 063837 (2010).
16. M. Tsang, "Cavity quantum electro-optics. II. input-output relations between traveling optical and microwave fields," Phys. Rev. A **84**, 043845 (2011).
17. L. Fan, C.-L. Zou, R. Cheng, *et al.*, "Superconducting cavity electro-optics: a platform for coherent photon conversion between superconducting and photonic circuits," Sci. Adv. **4**, eaar4994 (2018).
18. Y. Xu, A. A. Sayem, L. Fan, *et al.*, "Bidirectional electro-optic conversion reaching 1% efficiency with thin-film lithium niobate," arXiv (2020).
19. W. Jiang, C. J. Sarabalis, Y. D. Dahmani, *et al.*, "Efficient bidirectional piezo-optomechanical transduction between microwave and optical frequency," Nat. Commun. **11**, 1–7 (2020).
20. J. Verdú, H. Zoubi, C. Koller, *et al.*, "Strong magnetic coupling of an ultracold gas to a superconducting waveguide cavity," Phys. Rev. Lett. **103**, 043603 (2009).
21. L. A. Williamson, Y.-H. Chen, and J. J. Longdell, "Magneto-optic modulator with unit quantum efficiency," Phys. Rev. Lett. **113**, 203601 (2014).
22. L. Shao, M. Yu, S. Maity, *et al.*, "Microwave-to-optical conversion using lithium niobate thin-film acoustic resonators," Optica **6**, 1498–1505 (2019).
23. N. Fiaschi, B. Hensen, A. Wallucks, *et al.*, "Optomechanical quantum teleportation," Nat. Photonics **15**, 817–821 (2021).
24. X. Han, W. Fu, C. Zhong, *et al.*, "Cavity piezo-mechanics for superconducting-nanophotonic quantum interface," Nat. Commun. **11**, 3237 (2020).

25. C. Zhong, Z. Wang, C. Zou, *et al.*, "Proposal for heralded generation and detection of entangled microwave–optical-photon pairs," Phys. Rev. Lett. **124**, 010511 (2020).
26. M. Mirhosseini, A. Sipahigil, M. Kalaee, *et al.*, "Superconducting qubit to optical photon transduction," Nature **588**, 599–603 (2020).
27. M. Forsch, R. Stockill, A. Wallucks, *et al.*, "Microwave-to-optics conversion using a mechanical oscillator in its quantum ground state," Nat. Phys. **16**, 69–74 (2020).
28. J. Holzgrafe, N. Sinclair, D. Zhu, *et al.*, "Cavity electro-optics in thin-film lithium niobate for efficient microwave-to-optical transduction," Optica **7**, 1714–1720 (2020).
29. R. Sahu, W. Hease, A. Rueda, *et al.*, "Quantum-enabled operation of a microwave-optical interface," Nat. Commun. **13**, 1276 (2022).
30. B. M. Brubaker, J. M. Kindem, M. D. Urmey, *et al.*, "Optomechanical ground-state cooling in a continuous and efficient electro-optic transducer," Phys. Rev. X **12**, 021062 (2022).
31. L. Qiu, R. Sahu, W. Hease, *et al.*, "Coherent optical control of a superconducting microwave cavity via electro-optical dynamical back-action," Nat. Commun. **14**, 3784 (2023).
32. R. Sahu, L. Qiu, W. Hease, *et al.*, "Entangling microwaves with light," Science **380**, 718–721 (2023).
33. M. M. Wolf, D. Pérez-García, and G. Giedke, "Quantum capacities of bosonic channels," Phys. Rev. Lett. **98**, 130501 (2007).
34. A. P. Higginbotham, P. Burns, M. Urmey, *et al.*, "Harnessing electro-optic correlations in an efficient mechanical converter," Nat. Phys. **14**, 1038–1042 (2018).
35. W. Hease, A. Rueda, R. Sahu, *et al.*, "Bidirectional electro-optic wavelength conversion in the quantum ground state," PRX Quantum **1**, 020315 (2020).
36. C. M. Caves, "Quantum limits on noise in linear amplifiers," Phys. Rev. D **26**, 1817–1839 (1982).
37. S. M. Meenehan, J. D. Cohen, S. Gröblacher, *et al.*, "Silicon optomechanical crystal resonator at millikelvin temperatures," Phys. Rev. A **90**, 011803 (2014).
38. H. Zhao, W. D. Chen, A. Kejriwal, *et al.*, "Quantum-enabled continuous microwave-to-optics frequency conversion," arXiv (2024).
39. M. Zhang, C.-L. Zou, and L. Jiang, "Quantum transduction with adaptive control," Phys. Rev. Lett. **120**, 020502 (2018).
40. Z. Wang and L. Jiang, "Passive environment-assisted quantum transduction with GKP states," arXiv (2024).
41. S. Konno, W. Asavanant, F. Hanamura, *et al.*, "Logical states for fault-tolerant quantum computation with propagating light," Science **383**, 289–293 (2024).
42. S. Meesala, S. Wood, D. Lake, *et al.*, "Non-classical microwave–optical photon pair generation with a chip-scale transducer," Nat. Phys. **20**, 871–877 (2024).
43. J. Wu, C. Cui, L. Fan, *et al.*, "Deterministic microwave-optical transduction based on quantum teleportation," Phys. Rev. Appl. **16**, 064044 (2021).
44. H. Shi and Q. Zhuang, "Ultimate precision limit of noise sensing and dark matter search," npj Quantum Inf **9**, 27 (2023).
45. Z. Ou, "Quantum amplification with correlated quantum fields," Phys. Rev. A **48**, R1761–R1764 (1993).
46. M. Chekhova and Z. Ou, "Nonlinear interferometers in quantum optics," Adv. Opt. Photonics **8**, 104–155 (2016).
47. F. Hudelist, J. Kong, C. Liu, *et al.*, "Quantum metrology with parametric amplifier-based photon correlation interferometers," Nat. Commun. **5**, 3049 (2014).
48. S. Guha and B. I. Erkmen, "Gaussian-state quantum-illumination receivers for target detection," Phys. Rev. A **80**, 052310 (2009).
49. K. Wurtz, B. Brubaker, Y. Jiang, *et al.*, "Cavity entanglement and state swapping to accelerate the search for axion dark matter," PRX Quantum **2**, 040350 (2021).
50. S. Hao, H. Shi, C. N. Gagatsos, *et al.*, "Demonstration of entanglement-enhanced covert sensing," Phys. Rev. Lett. **129**, 010501 (2022).
51. Y. Jiang, E. P. Ruddy, K. O. Quinlan, *et al.*, "Accelerated weak signal search using mode entanglement and state swapping," PRX Quantum **4**, 020302 (2023).
52. K. A. Gilmore, M. Affolter, R. J. Lewis-Swan, *et al.*, "Quantum-enhanced sensing of displacements and electric fields with two-dimensional trapped-ion crystals," Science **373**, 673–678 (2021).
53. K. M. Backes, D. A. Palken, S. A. Kenany, *et al.*, "A quantum enhanced search for dark matter axions," Nature **590**, 238–242 (2021).
54. M. Xu, R. Cheng, Y. Wu, *et al.*, "Magnetic field-resilient quantum-limited parametric amplifier," PRX Quantum **4**, 010322 (2023).
55. J. Y. Qiu, A. Grimsmo, K. Peng, *et al.*, "Broadband squeezed microwaves and amplification with a josephson travelling-wave parametric amplifier," Nat. Phys. **19**, 706–713 (2023).
56. T. Eberle, V. Händchen, and R. Schnabel, "Stable control of 10 dB two-mode squeezed vacuum states of light," Opt. Express **21**, 11546–11553 (2013).
57. R. Nehra, R. Sekine, L. Ledezma, *et al.*, "Few-cycle vacuum squeezing in nanophotonics," Science **377**, 1333–1337 (2022).
58. Z. Yan, X. Jia, X. Su, *et al.*, "Cascaded entanglement enhancement," Phys. Rev. A **85**, 040305 (2012).
59. M. Wang, M. Zhang, Z. Qin, *et al.*, "Experimental preparation and manipulation of squeezed cat states via an all-optical in-line squeezer," Laser Photonics Rev. **16**, 2200336 (2022).
60. A. H. Safavi-Naeini and O. Painter, "Proposal for an optomechanical traveling wave phonon–photon translator," New J. Phys. **13**, 013017 (2011).
61. C. L. Rau, A. Kyle, A. Kwiatkowski, *et al.*, "Entanglement thresholds of doubly parametric quantum transducers," Phys. Rev. Appl. **17**, 044057 (2022).
62. S. Lloyd, "Capacity of the noisy quantum channel," Phys. Rev. A **55**, 1613–1622 (1997).
63. P. W. Shor, "The quantum channel capacity and coherent information," in Lecture notes, *MSRI Workshop on Quantum Computation* (2002).
64. I. Devetak, "The private classical capacity and quantum capacity of a quantum channel," IEEE Trans. Inf. Theory **51**, 44–55 (2005).
65. A. S. Holevo and R. F. Werner, "Evaluating capacities of bosonic Gaussian channels," Phys. Rev. A **63**, 032312 (2001).
66. C.-H. Wang, F. Li, and L. Jiang, "Quantum capacities of transducers," Nat. Commun. **13**, 6698 (2022).
67. J. Kong, F. Hudelist, Z. Ou, *et al.*, "Cancellation of internal quantum noise of an amplifier by quantum correlation," Phys. Rev. Lett. **111**, 033608 (2013).
68. X. Guo, X. Li, N. Liu, *et al.*, "Quantum information tapping using a fiber optical parametric amplifier with noise figure improved by correlated inputs," Sci. Rep. **6**, 30214 (2016).
69. C. Weedbrook, S. Pirandola, R. García-Patrón, *et al.*, "Gaussian quantum information," Rev. Mod. Phys. **84**, 621–669 (2012).
70. W. K. Wootters and W. H. Zurek, "A single quantum cannot be cloned," Nature **299**, 802–803 (1982).
71. C. W. Gardiner and M. J. Collett, "Input and output in damped quantum systems: quantum stochastic differential equations and the master equation," Phys. Rev. A **31**, 3761–3774 (1985).
72. L. McCuller, C. Whittle, D. Ganapathy, *et al.*, "Frequency-dependent squeezing for advanced LIGO," Phys. Rev. Lett. **124**, 171102 (2020).
73. W. Jia, V. Xu, K. Kuns, *et al.*, "Squeezing the quantum noise of a gravitational-wave detector below the standard quantum limit," Science **385**, 1318–1321 (2024).
74. M. Malnou, D. Palken, B. Brubaker, *et al.*, "Squeezed vacuum used to accelerate the search for a weak classical signal," Phys. Rev. X **9**, 021023 (2019).
75. W. P. Bowen and G. J. Milburn, *Quantum Optomechanics* (CRC press, 2015).
76. H. Vahlbruch, M. Mehmet, K. Danzmann, *et al.*, "Detection of 15 dB squeezed states of light and their application for the absolute calibration of photoelectric quantum efficiency," Phys. Rev. Lett. **117**, 110801 (2016).
77. T. Kashiwazaki, N. Takanashi, T. Yamashima, *et al.*, "Continuous-wave 6-dB-squeezed light with 2.5-THz-bandwidth from single-mode PPLN waveguide," APL Photonics **5**, 036104 (2020).
78. C. Zhong, X. Han, and L. Jiang, "Microwave and optical entanglement for quantum transduction with electro-optomechanics," Phys. Rev. Appl. **18**, 054061 (2022).

79. A. S. Holevo, "Entanglement-breaking channels in infinite dimensions," Probl. Inf. Transm. **44**, 171–184 (2008).
80. C. Zhong, M. Xu, A. Clerk, *et al.*, "Quantum transduction is enhanced by single mode squeezing operators," Phys. Rev. Res. **4**, L042013 (2022).
81. Z. Yang, M. Jahanbozorgi, D. Jeong, *et al.*, "A squeezed quantum microcomb on a chip," Nat. Commun. **12**, 4781 (2021).
82. J. H. Shapiro and N. Wong, "An ultrabright narrowband source of polarization-entangled photon pairs," J. Opt. B:Quantum Semiclassical Opt. **2**, L1–L4 (2000).